Preferred citation: S.B. Lindström, T. Uesaka and U. Hirn. Evolution of the paper structure along the length of a twin-wire former. In **Advances in Pulp and Paper Research, Oxford 2009**, *Trans. of the XIVth Fund. Res. Symp. Oxford, 2009*, (S.J. I'Anson, ed.), pp 207–245, FRC, Manchester, 2018. DOI: 10.15376/frc.2009.1.207.

EVOLUTION OF THE PAPER STRUCTURE ALONG THE LENGTH OF A TWIN-WIRE FORMER

Stefan B. Lindström[1], Tetsu Uesaka[1] and Ulrich Hirn[2]*

[1]Department of Natural Sciences, Engineering and Mathematics, Mid Sweden University, Holmgatan 10, 851 70 Sundsvall, Sweden
[2]Institute of Paper, Pulp and Fibre Technology, Graz University of Technology, Kopernikusgasse 24, 8010 Graz, Austria

ABSTRACT

A particle-level numerical model is used to simulate forming with a twin-wire former configuration. The development of the paper structure along the length of the former is observed to explain the effects of the dewatering elements on the paper structure at different jet-to-wire speed ratios, consistencies, and target basis weights. The simulations indicate that most of the structure development takes place in the initial part of forming (forming roll) and, in some instances, at the drop to atmospheric pressure after the forming roll. Dramatic effects on the through-thickness fibre orientation anisotropy are observed when the consistency is varied by changing the jet thickness, while changes in basis weight had less impact. The through-thickness concentration gradient was almost uniform throughout the forming process, except in the lower range of typical papermaking consistencies. This indicates that the dewatering mechanism is normally thickening, rather than filtration.

*Current affiliation: FPInnovations – Paprican Division, 570 St. John Boulevard, Pointe-Claire, Quebec, Canada H9R-3J9.

1 INTRODUCTION

Controlling formation and fibre orientation anisotropy of the paper structure is essential for the optimisation of product performance. Many important features of the paper structure develop in the forming section of the paper machine, and it is through the design of the forming process that the paper structures can be controlled. However, the development of the paper structures occurs at the length scales of fibres, which are difficult to access in on-line measurements. Particle-level simulations of forming have the potential to predict the evolution of the paper structure, thus uncovering information critical for a more systematic forming process design.

With the emerging technique of particle-level simulation of forming [1], greater detail of the evolving paper structure becomes available for analysis along the length of the forming section. This opens up the possibility to investigate a variety of questions critical to papermakers. In this paper, we are specifically concerned with the questions:

- What are the effects of individual drainage elements on the paper microstructures?
- How does changes in the basic parameters, *i.e.* grammage and consistency, modify the paper microstructures?

In order to answer these questions, we investigate the development of the through-thickness fibre length distribution, and the through-thickness fibre orientation distribution in a roll–blade gap former.

An illustration of the former configuration examined in this study is provided in Fig. 1. This configuration is similar to the one used in the Voith DuoFormer™ TQv [2]. The headbox ejects a wide and thin (~1 cm) jet of fibre suspension, which impinges on two moving wires. The wires are running under tension, so that a pressure develops in the mix between them as they pass the forming roll. Fluid is thus drained through the wires, while most of the fibrous material remain between the wires due to the geometrical constraints of the wire yarns. Further downstream, other types of drainage elements continue to drain fluid from the mix: The blades induce intermittent pressure pulses into the mix, draining fluid as well as causing an oscillating flow relative to the wires in the machine direction. The suction box and the couch roll apply a vacuum to drain fluid. In addition, a structural pressure develops over the couch roll due to the wire tension.

Previously, forming theories usually assume that the fibre suspension in the forming section consists of a homogeneous fluid (or a homogeneous fluid and a permeable continuum solid) and is then formulated by coupling the standard conservations laws for multiphase flow, Darcy's law [3], and a choice

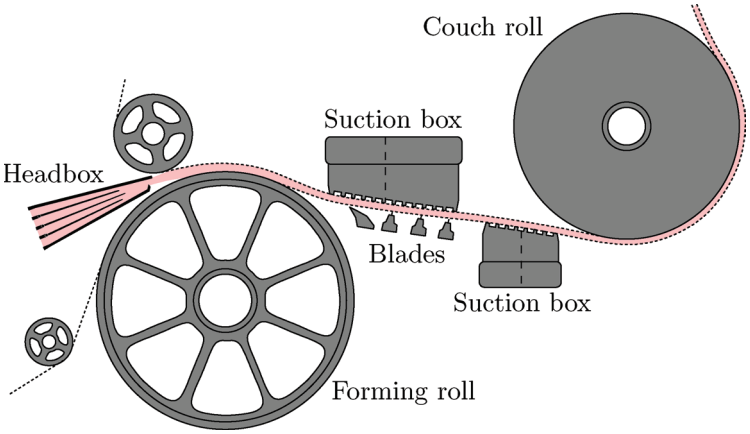

Figure 1. Schematic illustration of a roll–blade gap former. The headbox nozzle ejects a thin wide jet of pulp mix onto two permeable wires (dotted lines). The tension of the top wire provides drainage pressure over the roll. The blades induce pressure pulses in the mix, which intermittently push fluid through the wires. Suction boxes drain fluid by applying vacuum, as do the couch roll.

of solidity-dependant constitutive law for the stress–strain relation of pulp fibre networks [4]. This approach was taken by Bando *et al.* [5] to model the pulsating flow of a roll-blade former, and by Martinez [6] to model dewatering on a forming roll. Lobosco and co-workers applied a similar uniaxial pressure model to a roll–blade former [7]. The modelling framework was expanded by Holmqvist *et al.* [8] to include machine directional flow. There are, however, some fundamental difficulties with these forming models. Particularly, the continuum assumption on which all the basic equations rely. The inherent length scale of the pulp mix is, at least, in the order of the fibre length (1–3 mm), probably even greater due to flocculation. Therefore, the representative volume element must be *much* greater than the fibre length, and consequently, greater than the thickness of the jet. Moreover, microscale effects, such as the limited fibre mobility, fibre orientation, flocculation and deflocculation, are not captured with the continuum assumption due to its limited resolution.

Another approach is to formulate the problem on a particle level. The first attempt to recreate the fibre network structure of paper with a computer model was presented by Niskanen and Alava [9]. In this, so called, PAKKA model, flexible fibres are randomly deposited on a substrate, one at a time. A three-dimensional structure is obtained which captures some of the statistical

properties of real fibre networks. To account for effects of the forming fabric, Barratte *et al.* [10] introduced a forming fabric geometry onto which fibres were deposited or rejected. However, these fibre deposition models do not consider the dynamics of the forming section, and cannot predict important effects of the former on the paper structures. Switzer *et al.* [11] simulated the dynamics of handsheet-making using the fibre suspension model of Schmid *et al.* [12], which integrates the motion of flexible fibres in a prescribed Stokes flow. The validity range of that model does not include the flow conditions of industrial forming operations, nor the important two-way coupling between the fibres and the suspending medium.

Building on the fibre suspension model proposed by Schmid, Switzer, and Klingenberg [12], Lindström and Uesaka presented a new particle-level fibre suspension model, whose validity was expanded into a much wider range, including the flow conditions of forming in modern paper machines [13, 14]. The new model considers inert, flexible fibres of various equilibrium shapes flowing and interacting with each other, and with the surrounding fluid medium through a two-way coupling. The model has also been employed in simulation of twin-wire forming [1], taking into account all relevant length scales of the flow down to the fibre diameter. The issues of dewatering and fibre network development are both handled in this single modelling framework. It was shown that the model captures well the essential features of the forming effects on the paper structure (fibre orientation anisotropy, network three-dimensionality, and formation).

In this work, we investigate *how* the paper structure develops during forming under different operating conditions, and *where* in the former this structural development takes place. This information is equally critical for the design of the forming section and the optimisation of the paper structure through tuning of the process parameters.

A brief overview of the fibre suspension model is given in Sec. 2. It also describes how multi-scale modelling can be applied to the flow in the forming section, in order to reduce the computational demand and maintain reasonable execution time for simulations. Section 3 includes a description of how a fibre analyser and other measurements performed at the paper mill have been used to formulate the initial conditions and process parameters of the simulations. The simulation results are presented in Sec. 4, including analyses of the development of the paper structure along the length of the forming section, as well as a comparison between the simulated sheets and sample sheets obtained from the paper mill. The last section 5 summarises the most important new findings of this investigation.

2 THEORY

The particle-level model for forming is based on a fibre suspension model which can be used to integrate the equations of motion for the coupled system of fibres and fluid. A detailed account of the suspension model is given in Ref. [13]. This section briefly describes the suspension model, and more thoroughly how the suspension model is applied to forming.

2.1 Fibre suspension model

The fibre suspension model integrates the motion of flexible fibres and a Newtonian fluid medium in a box-shaped domain Ω. A Cartesian coordinate frame Γ with base vectors $\hat{e}_1$, $\hat{e}_2$, and $\hat{e}_3$ is used, its three axes aligned with the sides of Ω.

2.1.1 Fluid model

The fluid medium is assumed to be incompressible with a constant density ρ and viscosity η. The motion of the fluid is described by the three-dimensional, incompressible Navier–Stokes equations. In this work, we use the finite difference scheme proposed by E and Liu [15], which is based on the vorticity–vector potential form of the Navier–Stokes equations:

$$\frac{\partial \boldsymbol{\xi}}{\partial t} = \nabla \times (\boldsymbol{v} \times \boldsymbol{\xi}) + \frac{1}{\rho} \nabla \times \nabla \cdot \boldsymbol{\tau} + \frac{1}{\rho} \nabla \times \boldsymbol{F}^{\mathrm{b}} \tag{1a}$$

$$\boldsymbol{\tau} = \eta \left[\nabla \boldsymbol{v} + (\nabla \boldsymbol{v})^{\mathrm{T}} \right] \tag{1b}$$

$$\boldsymbol{\xi} = \nabla \times \boldsymbol{v} \tag{1c}$$

$$\boldsymbol{v} = \nabla \times \boldsymbol{\Phi} \tag{1d}$$

$$\Delta \boldsymbol{\Phi} = -\boldsymbol{\xi} \tag{1e}$$

$$\boldsymbol{v}(\boldsymbol{x}, 0) = \boldsymbol{v}_0(\boldsymbol{x}), \tag{1f}$$

where $\boldsymbol{\xi}$ is the vorticity, $\boldsymbol{\tau}$ is the viscous stress tensor, $\boldsymbol{v}$ is the velocity, $\boldsymbol{v}_0$ is the initial velocity, $\boldsymbol{\Phi}$ is the vector potential, and $\boldsymbol{F}^{\mathrm{b}}$ is the body force density. Here, $\boldsymbol{F}^{\mathrm{b}}$ includes the pressure exerted by the fibre phase, as well as immersed boundaries, on the fluid. The boundary conditions for planar fluid–void interfaces are

$$\hat{\boldsymbol{n}} \cdot \boldsymbol{v} = 0 \tag{2a}$$

$$\frac{\partial}{\partial \hat{\boldsymbol{n}}}(\hat{\boldsymbol{n}} \times \boldsymbol{v}) = \boldsymbol{0} \tag{2b}$$

$$\hat{\boldsymbol{n}} \times \boldsymbol{\Phi} = \boldsymbol{0} \tag{2c}$$

$$\frac{\partial}{\partial \hat{\boldsymbol{n}}}(\hat{\boldsymbol{n}} \cdot \boldsymbol{\Phi}) = 0 \tag{2d}$$

$$\hat{\boldsymbol{n}} \times \boldsymbol{\xi} = \boldsymbol{0} \tag{2e}$$

$$\frac{\partial}{\partial \hat{\boldsymbol{n}}}(\hat{\boldsymbol{n}} \cdot \boldsymbol{\xi}) = 0, \tag{2f}$$

where $\hat{\boldsymbol{n}}$ is the outward normal unit vector. Condition (2a) ensures that no fluid flows over the boundary, and condition (2b) follows from the vanishing shear stress at the free-slip boundary. Boundary conditions (2c)–(2f) are derived (see Ref. [16]). A second order spatial discretisation on a regular grid, and a third order time discretisation were employed to integrate Eqs. (1a)–(1f). Note that the third order derivatives of the velocity in Eq. (1a) can be replaced by second order derivatives of the vorticity after some manipulation, thus enabling the use of an essentially compact scheme for the spatial discretisation.

The subgrid turbulence model proposed by Lesieur and Métais [17] was included in order to allow for the calculation of large Reynolds number flows at a reasonable cell size of the spatial discretisation. This is a Reynolds-average approach in which the subgrid turbulence is accounted for by adding the eddy viscosity

$$\eta_{\mathrm{t}}(\boldsymbol{x}, t) = 0.105 C_{\mathrm{K}}^{-3/2} \rho \Delta x \sqrt{F_2(\boldsymbol{x}, t)}, \tag{3}$$

to the true viscosity of the medium. Here, $C_K \approx 1.4$ is the Kolmogorov constant, $\boldsymbol{x}$ is the position, Δx is the cell size of the spatial discretisation, and $\boldsymbol{F}_2$ is the local second order velocity structure function defined by

$$F_2(\boldsymbol{x}, t) = \left\langle \|\boldsymbol{v}(\boldsymbol{x}, t) - \boldsymbol{v}(\boldsymbol{x} + \boldsymbol{\rho}, t)\|^2 \right\rangle_{\|\boldsymbol{\rho}\| = \Delta x}. \tag{4}$$

On a regular grid, equation (4) is efficiently approximated by using a local statistical average over the six closest grid points. The Kolmogorov energy spectrum, $E(k)$, $\propto k^{-5/3}$, for isotropic turbulence is well reproduced with this subgrid turbulence model [17] (k denotes the wave number). It should be

noted that the presence of fibres introduces non-isotropic structures in the suspension, suggesting that the dissipation may be different from the isotropic case. The development of a subgrid turbulence model which includes the effects of the immersed fibres on subgrid scales is, however, not within the scope of this work.

During drainage, the fluid interacts with the forming fabrics, which are weft from yarns of much larger diameter than wood fibres. The Immersed Boundary Method (IBM) was proposed by Peskin [8] for modelling complex moving boundaries inside the computational domain. With the IBM, the volume occupied by the immersed objects are included in the CFD computations and a forcing term is added at their boundaries to enforce the no-slip condition. Suppose a body occupies the region $\Omega_i^{\mathrm{ib}}(t)$, and that its velocity is $\boldsymbol{v}_i^{\mathrm{ib}}(\boldsymbol{x}, t)$: $\Omega_i^{\mathrm{ib}} \to \mathbb{R}^3$. The body exerts a traction $\boldsymbol{t}_i^{\mathrm{ib}}$ on the fluid at the interface. Note that $\boldsymbol{t}_i^{\mathrm{ib}}$ is the sum of the traction on the outer and inner side of the virtual boundary. In this work, we employ a variant of the IBM with direct forcing [19]. The body force density of Eq. (1a) is divided into two components:

$$\boldsymbol{F}^{\mathrm{b}} = \boldsymbol{F}^{\mathrm{p}} + \sum_i \boldsymbol{F}_i^{\mathrm{ib}}, \tag{5}$$

where $\boldsymbol{F}^{\mathrm{p}}$ represents the force density exerted on the fluid by the particles, while $\boldsymbol{F}_i^{\mathrm{ib}}$ is the force density exerted by the ith immersed boundary:

$$\boldsymbol{F}_i^{\mathrm{ib}}(\boldsymbol{x}) = \iint_{\partial\Omega_i^{\mathrm{ib}}} \boldsymbol{t}_i^{\mathrm{ib}} \delta(\boldsymbol{x} - \boldsymbol{x}_i^{\mathrm{ib}}) \mathrm{d}S, \tag{6}$$

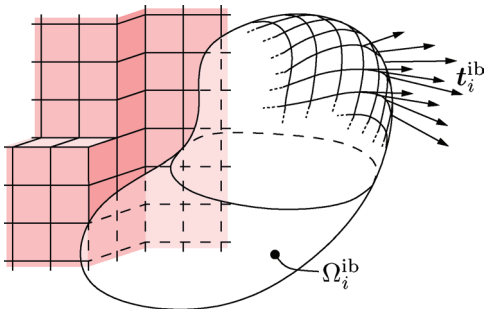

Figure 2. The Immersed Boundary Method. The ith immersed object occupies the domain Ω^{ib}. Its boundary $\partial\Omega_i^{\mathrm{ib}}$ is discretised, and a traction $\boldsymbol{t}_i^{\mathrm{ib}}$ is computed at the surface grid points. This force is then mapped onto the regular grid of the fluid discretisation.

where $\boldsymbol{x}_i^{\mathrm{ib}} \in \partial\Omega_i^{\mathrm{ib}}$, and $\mathrm{d}S$ is a surface element. Consider the region ω_i^{ib} consisting of all points whose distance to the boundary $\partial\Omega_i^{\mathrm{ib}}$ is less than half the cell size of the discretisation $\frac{1}{2}\Delta x$. Then, ω_i^{ib} is a shell of thickness Δx enclosing the boundary. From Newton's second law, we obtain the force density $\boldsymbol{F}_i^{\mathrm{ib}}$ required to accelerate the fluid inside ω_i^{ib} to the velocity $\boldsymbol{v}_i^{\mathrm{ib}}$ in one time step

$$\boldsymbol{F}_i^{\mathrm{ib}} \approx \begin{cases} -\rho\boldsymbol{v} \times \boldsymbol{\xi} - \nabla \cdot \boldsymbol{\tau} - \boldsymbol{F}^{\mathrm{p}} - \sum_{k \neq i} \boldsymbol{F}_k^{\mathrm{ib}} + \frac{\rho}{\Delta t}\left(\boldsymbol{v}_i^{\mathrm{ib}} - \boldsymbol{v}\right), & \boldsymbol{x} \in \omega_i^{\mathrm{ib}} \\ \boldsymbol{0}, & \text{otherwise.} \end{cases} \tag{7}$$

The force density $\boldsymbol{F}_i^{\mathrm{ib}}$ must overcome the dynamic and viscous forces of the fluid, as well as effects of the particle pressure. If there is a velocity difference $\boldsymbol{v}_i^{\mathrm{ib}}(t) - \boldsymbol{v}(t)$, the last term of Eq. (7) accelerates the fluid to the prescribed velocity at time $t + \Delta t$. Note that the sum of the contributions from other immersed boundaries is eliminated when the domains ω_k^{ib}, $\forall k$ are disjoint. Eliminating $\boldsymbol{F}_i^{\mathrm{ib}}$ from Eqs. (6) and (7) renders an expression for the traction $\boldsymbol{t}_i^{\mathrm{ib}}$, which, in this work, is represented by a grid of point forces. A mapping procedure is used to add the grid of forces to the body force term $\boldsymbol{F}^{\mathrm{b}}$ of Eq. (1a) (see Ref. [13]).

2.1.2 Fibre model

Fibres are modelled as chains of cylinder-shaped fibre segments with spherical caps, as illustrated in Fig. 3. The spherical caps make the calculation of distance between fibre segments more efficient, as compared to plane caps, thus significantly reducing the computational demand in the calculation of distance-dependant interactions. The length of the fibre is denoted by L and

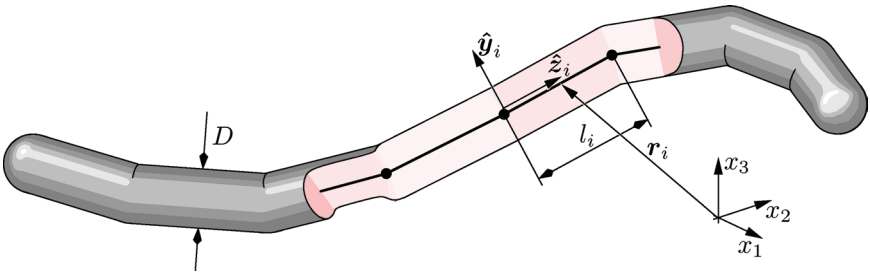

Figure 3. Fibres are modelled as chains of fibre segments with spherical caps. Each segment indexed i is associated with a segment length l_i, a position vector $\boldsymbol{r}_i$, a direction vector $\hat{\boldsymbol{z}}_i$, and an up-direction vector $\hat{\boldsymbol{y}}_i$.

the diameter by D. A fibre segment indexed i is associated with a segment length l_i, a position vector $\boldsymbol{r}_i$ to the segment centroid, a direction unit vector $\hat{\boldsymbol{z}}_i$ pointing along the length of the segment, and an up-direction unit vector $\hat{\boldsymbol{y}}_i$. That is, a local, Cartesian coordinate system Γ_i with base vectors $\hat{\boldsymbol{x}}_i = \hat{\boldsymbol{y}}_i \times \hat{\boldsymbol{z}}_i$, $\hat{\boldsymbol{y}}_i$, and $\hat{\boldsymbol{z}}_i$ is fixed to segment i. The equilibrium shape of the fibre is represented by a set of affine transforms mapping each Γ_i^{eq} onto $\Gamma_{i+1}^{\mathrm{eq}}$. Here, Γ_i^{eq} is the local coordinate system of the equilibrium state. Storing the equilibrium shape makes possible the calculation of the restoring moments in the fibre segment joints.

Applying Newton's second law for translational motion to segment i gives

$$m_i \ddot{\boldsymbol{r}}_i = \boldsymbol{F}_i^{\mathrm{h}} + \boldsymbol{X}_{i+1} - \boldsymbol{X}_i + \sum_j \boldsymbol{f}_{ij}, \tag{8}$$

where m_i is the mass, $\boldsymbol{F}_i^{\mathrm{h}}$ is the drag force, $\boldsymbol{X}_i$ is the force of segment i acting on adjacent segment $i-1$, and $\boldsymbol{f}_{ij}$ is the interaction force exerted on segment i by segment j of some other fibre, or by a non-adjacent segment of the same fibre. Similarly, Newton's second law for rotational motion yields

$$\frac{\partial}{\partial t}(\boldsymbol{I}_i \cdot \boldsymbol{\omega}_i) = \boldsymbol{T}_i^{\mathrm{h}} + \boldsymbol{Y}_{i+1} - \boldsymbol{Y}_i + \frac{l_i}{2}\hat{\boldsymbol{z}}_i \times (\boldsymbol{X}_{i+1} + \boldsymbol{X}_i) + \sum_j \boldsymbol{t}_{ij}, \tag{9}$$

where $\boldsymbol{I}_i$ is the tensor of inertia of segment i with respect to Γ, $\boldsymbol{\omega}_i$ is the angular velocity, $\boldsymbol{T}_i^{\mathrm{h}}$ is the hydrodynamic torque, $\boldsymbol{Y}_i$ is the torsion and bending moment exerted on segment $i-1$ by segment i, and $\boldsymbol{t}_{ij}$ is the torque caused by the contact force $\boldsymbol{f}_{ij}$. The system of equations is closed by adding connectivity constraints. The requirement that adjacent segment ends must coincide gives

$$\dot{\boldsymbol{r}}_i - \dot{\boldsymbol{r}}_{i+1} + \frac{1}{2} l_i \boldsymbol{\omega}_i \times \hat{\boldsymbol{z}}_i + \frac{1}{2} l_{i+1} \boldsymbol{\omega}_{i+1} \times \hat{\boldsymbol{z}}_{i+1} = \boldsymbol{0}. \tag{10}$$

Equations (8)–(10) can be solved for the velocities and angular velocities of the fibre segments for one fibre at a time, if the dynamics of the fibre contacts are properly handled [1].

2.1.3 Fibre–fluid and fibre–fibre interactions

The fibre suspension model takes into account the two-way interactions between the particles and the fluid, as well as inter-particle collisions. This momentum balance between the phases and within the particle phase is often referred to as the four-way coupling.

The dynamics of a circular cylinder in a linear flow gradient of a Newtonian fluid is well known from analytical [20, 21, 22] as well as experimental studies [23, 24]. The hydrodynamic drag force $\boldsymbol{F}_i^{\mathrm{h}}$ and torque $\boldsymbol{T}_i^{\mathrm{h}}$ on fibre segment i, due to the flow velocity $\boldsymbol{v}$, can be expressed as [25]

$$\boldsymbol{F}_i^{\mathrm{h}} = \boldsymbol{A}_i^{\mathrm{h}} \cdot (\boldsymbol{v}(\boldsymbol{r}_i) - \dot{\boldsymbol{r}}_i) \tag{11a}$$

$$\boldsymbol{T}_i^{\mathrm{h}} = \boldsymbol{C}_i^{\mathrm{h}} \cdot (\boldsymbol{\Omega}(\boldsymbol{r}_i) - \boldsymbol{\omega}_i) + \boldsymbol{H}_i^{\mathrm{h}} : \dot{\boldsymbol{\gamma}}(\boldsymbol{r}_i), \tag{11b}$$

where $\boldsymbol{\Omega} = \frac{1}{2} \nabla \times \boldsymbol{v}$ is the angular velocity of the fluid, and $\dot{\gamma} = \frac{1}{2} (\nabla \boldsymbol{v} + (\nabla \boldsymbol{v})^{\mathrm{T}})$ is the rate of strain tensor. The hydrodynamic resistance tensors $\boldsymbol{A}_i^{\mathrm{h}}$, $\boldsymbol{C}_i^{\mathrm{h}}$, and $\boldsymbol{H}_i^{\mathrm{h}}$ are defined in Ref. [13]. If $\boldsymbol{v}$ is not a linear flow gradient, Eqs. (11a) and (11b) represent an approximation of the hydrodynamic interactions based on the multipole expansion of $\boldsymbol{v}$ around the centroid of the fibre segment. Higher order terms are neglected.

With Eqs. (11a) and (11b), the local flow disturbance caused by the fibre segment is accounted for, but not explicitly included in the velocity field $\boldsymbol{v}$. The fluid flow solver is responsible for capturing the flow structures at length scales greater than the fibre segment length. Therefore, the maximum cell size Δx of the discretisation of $\boldsymbol{v}$ is in the order of the segment length. It was shown numerically in Ref. [13] that it is sufficient to choose the cell size equal to the fibre segment length in order to predict the self-interactions of isolated fibres.

The momentum conservation between the fibre and fluid phases is enforced, simply by adding the reaction forces $-\boldsymbol{F}_i^{\mathrm{h}}$ and reaction torques $-\boldsymbol{T}_i^{\mathrm{h}}$ as a grid of point forces to the body force density $\boldsymbol{F}^{\mathrm{b}}$ of Eq. (1a) (see Ref. [14]).

All subgrid interactions between fibre segments are modelled using the interaction force $\boldsymbol{f}_{ij}$, defined by

$$\boldsymbol{f}_{ij} = \boldsymbol{F}_{ij}^{\mathrm{n}} + \boldsymbol{F}_{ij}^{\mathrm{f}} + \boldsymbol{F}_{ij}^{\mathrm{l}}, \tag{12}$$

where $\boldsymbol{F}_{ij}^{\mathrm{n}}$ is the normal force, $\boldsymbol{F}_{ij}^{\mathrm{f}}$ is the frictional force, and $\boldsymbol{F}_{ij}^{\mathrm{l}}$ is the lubrication force. Evidently, potential forces can be included with ease. The interaction force also gives rise to a torque $\boldsymbol{t}_{ij} = \boldsymbol{j}_{ij} \times \boldsymbol{f}_{ij}$, where $\boldsymbol{j}_{ij}$ is a vector from the centroid of segment i to the point of contact on the fibre surface.

The terms of the expression for the interaction force (12) does not numerically well-behave for ideal particles, *i.e.* fibre segments of perfectly smooth surfaces. The lubrication force would be singular, and the normal force would be discontinuous. Therefore, we introduce a measure δ_{s} for the surface roughness, the typical amplitude of the surface asperities.

Yamamoto and Matsuoka [26] and Schmid *et al.* [12] suggested that the normal forces should be taken as a repulsive force, exponentially increasing with the fibre surface interpenetration. We employ their mode, but also include a linear elastic model at the scale of the surface roughness:

$$\boldsymbol{F}_{ij}^{\mathrm{n}} \cdot \hat{\boldsymbol{n}}_{ij} = \begin{cases} -F_0 \exp\left(-\frac{H_{ij}+\delta_{\mathrm{s}}}{H_0}\right), & H_{ij} \leq -\delta_{\mathrm{s}} \\ -F_0 \left(\frac{1}{2} - \frac{H_{ij}}{2\delta_{\mathrm{s}}}\right) & , -\delta_{\mathrm{s}} < H_{ij} \leq \delta_{\mathrm{s}} \\ 0 & , H_{ij} > \delta_{\mathrm{s}}, \end{cases} \tag{13}$$

where $\hat{\boldsymbol{n}}_{ij}$ is the outward normal unit vector of segment i at the point of interaction, H_{ij} is the gap between the two segments, which may be negative in the event of an overlap, and F_0 and H_0 are constants. The choice of constants is discussed in Ref. [13]. The frictional force is directed to counteract the relative tangential motion of fibre segments. It is assumed that the fibres are always slipping, and that

$$|\boldsymbol{F}_{ij}^{\mathrm{f}}| = \mu_{\mathrm{f}} |\boldsymbol{F}_{ij}^{\mathrm{n}}|, \tag{14}$$

where μ_{f} is the coefficient of interparticle friction.

Yamane *et al.* [27] derived the leading order term of the lubrication force between two infinite circular cylinders. Here, since lubrication breaks down at particle separations smaller than the surface roughness [28], a lubrication cut-off was included at $H_{ij} = \delta_{\mathrm{s}}$. In addition, an upper lubrication cut-off at $H_{ij} = \overline{D}_{ij} = 2/(1/D_i + 1/D_j)$ was included because of the validity limit of the lubrication approximation:

$$\boldsymbol{F}_{ij}^{\mathrm{l}} \cdot \hat{\boldsymbol{n}}_{ij} = \frac{3\pi}{\sin\theta} \eta \overline{D}_{ij}^2 \dot{H}_{ij} \cdot \begin{cases} 1/\delta_{\mathrm{s}} & , H_{ij} \leq \delta_{\mathrm{s}} \\ 1/H_{ij} & , \delta_{\mathrm{s}} < H_{ij} \leq \overline{D}_{ij} \\ 0 & , H_{ij} > \overline{D}_{ij}. \end{cases} \tag{15}$$

Here, θ is the contact angle. The tangential lubrication is $\mathbb{O}(\ln(\overline{D}_{ij}/H_{ij}))$, and was neglected in this contact model. The finite length of the fibre segments can be accounted for, as described in Ref. [13].

2.2 Forming model

With the fibre suspension model outlined above, a model for forming may be formulated. Even though the computational intensity has been significantly reduced by only accounting for subgrid flow features implicitly, it is still a challenge to deal with the large number of particles whose motion may be

integrated throughout the forming process. In addition, the length scale of the geometry of the headbox is too great to allow for a particle-level simulation within a reasonable time frame. Therefore, these simulations are focused on the jet and the drainage zone.

2.2.1 Separation of scales

The headbox ejects a thin, plane jet, whose thickness varies in the flow direction (see Fig. 4). Near the point of impingement at the wires, there may be significant secondary flows, as well as instabilities in the free surfaces of the jet. On the forming roll, fluid is drained through both wires at different rates. The complex interactions between the two-phase flow and the moving boundary of the wires give rise to pressure variations in the machine direction. The pressure variations, in turn, induce acceleration or deceleration of the mix in the machine direction. The pressure, the dewatering rate, and the flow are coupled, so that the conditions downstream affect the dewatering upstream and *vice versa*. In this sense, the flow has global qualities. Therefore, to predict the flow, it is necessary to take the whole flow geometry into account. At the same time, since the particle size is of the same order as the jet thickness, it is not possible to employ a continuum approximation for the suspension. Consequently, the dynamics of the system must be captured at particle length scales as well as the length scale of the entire flow geometry; a formidable problem from the point of computational intensity.

To address these computational issues, the problem is separated into two ranges of length scales: The *large scale flow* for length scales much greater than the jet thickness, and the *small scale flow* for length scales in the order of the jet thickness and below. Then, we may exploit the fact that the large scale flow is almost one-dimensional. The small scale flow can be integrated inside a box-shaped domain moving with the wires.

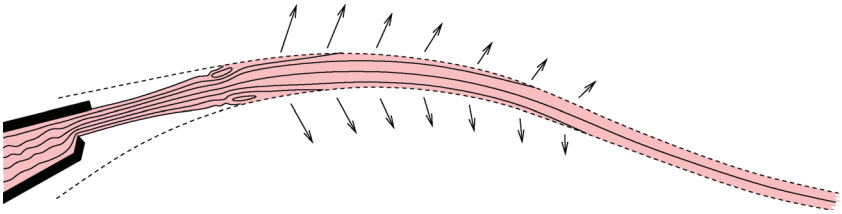

Figure 4. Complex flow inside the former. The headbox ejects a jet, which first contracts and then expands before it impinges on the wires. The flow is three-dimensional at length scales smaller than the jet thickness, and two-dimensional at scales larger than the jet thickness.

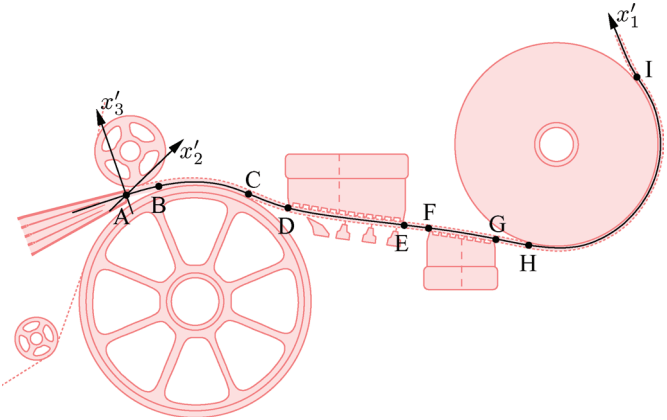

Figure 5. A coordinate system Γ' is introduced, where the x_1' axis runs along the length of the web, the x_2' axis points in the cross direction, and the x_3' axis is directed through the thickness of the web, pointing away from the forming roll.

As illustrated in Fig. 5, a curvilinear coordinate system Γ' is introduced, with its origin fixed at the headbox nozzle. The x_1' axis points in the machine direction (MD) and follows the curvature of the web. The x_2' axis points in the cross direction (CD). The x_3' coordinate vector is perpendicular to the x_1' and x_2' coordinate vectors, so that the x_3' axis points in the thickness direction (ZD), away from the forming roll. A moving Cartesian coordinate system Γ with coordinates x_1, x_2, and x_3 is defined, so that $x_1 = x_1' - u_w t$, $x_2 = x_2'$, and $x_3 = x_3'$. Here, u_w is the wire speed. The domain of computations Ω for small scale flow is stationary with respect to Γ, and thus moves along the web with the speed of the wires. Henceforth, Γ' will be used for modelling the large scale flow, while Γ is suitable for modelling the small scale flow.

Clearly, Γ is an accelerated coordinate frame due to the curvature of the x_1' axis. The centripetal acceleration enters the Navier–Stokes equations through the body force term $\boldsymbol{F}^{\mathrm{b}}$, but when the curl of $\boldsymbol{F}^{\mathrm{b}}$ is taken in Eq. (1a) the contribution from the centripetal acceleration vanishes. That is, with the vorticity–vector potential formulation, the effects of the curvature will be included in the boundary conditions rather than the equations of motion.

2.2.2 Small scale flow

Flow features at the scales of the jet thickness and below are computed using the fibre suspension model previously described in Sec. 2.1. Fibres and fluid are contained within the box-shaped domain Ω, which moves with Γ.

Between points A and B along the x_1' axis in Fig. 5, the suspension travels in free air. Free-slip boundary conditions are applied to the boundary planes of Ω with surface normal $\pm\hat{\boldsymbol{e}}_3$. That is, the suspension–air interfaces are restricted to planes in this model. Periodic boundary conditions are applied to the other boundaries of Ω.

At the point B, two model wires are introduced outside the domain Ω used in the simulation of the jet, their yarn surfaces tangent to the free-slip boundaries of Ω. All fibrous material is thus contained between the wires at this point. The domain is then expanded in the $\pm x_3$ directions so that it encloses both wires. The flow geometry at point B is illustrated in Fig. 6.

The wires are modelled as a set of interwoven yarns, where each yarn is modelled using the fibre model of Sec. 2.1.2 with infinite stiffness. Because the yarns generally have a much larger diameter than the fibres of the suspension, the interactions between the yarns and suspending medium are modelled using the IBM (see Sec. 2.1.1).

The bottom and top wire positions along the x_3 direction are denoted by h_1 (x_1') and h_2 (x_1'), respectively. The volumetric fluxes of suspension through the bottom and top wires are $\dot{h}_1$ (x_1') and $-\dot{h}_2$ (x_1'). It is described in later Sec. 3 how these functions can be approximated using machine measurements and previous models.

The average mix-to-wire speed difference Δu_{mw} (x_1') is not given by the small scale flow model. Instead, it is supplied by the large scale flow model described in the next section.

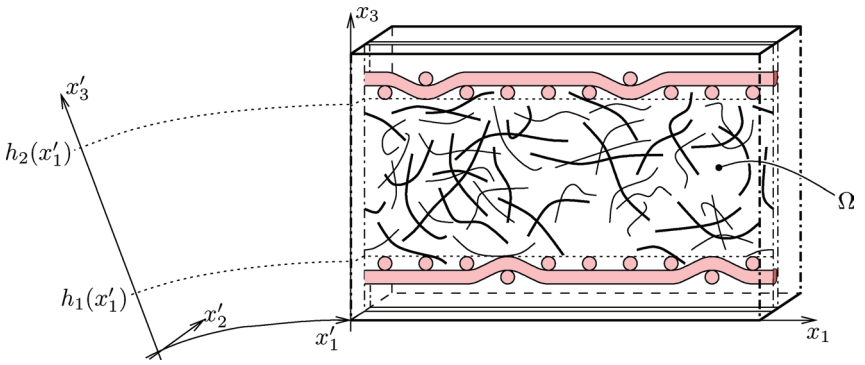

Figure 6. Drainage simulation with the small scale flow model. Two wire yarns are introduced with the fibre suspension in between. The motion of the wires is controlled by h_1 (x_1') and h_2 (x_1').

2.2.3 Large scale flow

The large scale flow is modelled in one dimension with the spatial coordinate x_1' of the Γ' coordinate frame. Since the free surface flow of the jet is neglected in this model, there is no change in average momentum or amount of material in the jet. After the impingement point B, however, momentum may be added to the mix through the traction of the wires, and fluid and particles escape from the mix through the voids of the wires.

The physical state of the large scale flow is described by the mix-to-wire speed difference $\Delta u_{\mathrm{mw}}(x_1')$, the average solids concentration by volume $c(x_1')$, and the hydrodynamic pressure in the mix $P_{\mathrm{m}}(x_1')$. To relate the physical state of the large scale flow to that of the small scale flow, we define the domain of the mix between the wires in the Γ coordinate frame: $\Omega_{\mathrm{m}} = \{\boldsymbol{x} : h_1(x_1') \le x_3 \le h_2(x_1')\}$, and describe the physical state at the point x_1' by the mix-to-wire speed difference

$$\Delta u_{\mathrm{mw}}(x_1') = \frac{1}{V_{\Omega_{\mathrm{m}}}} \iiint_{\Omega_{\mathrm{m}}} \boldsymbol{v}(\boldsymbol{x}, x_1'/u_{\mathrm{w}}) \cdot \hat{\boldsymbol{e}}_1 \mathrm{d}x_1 \mathrm{d}x_2 \mathrm{d}x_3, \tag{16}$$

and the average solids concentration by volume c in Ω_{m} using a similar averaging. Here, $V_{\Omega_{\mathrm{m}}}$ is the volume of Ω_{m}. Note that the integration in Eq. (16) is performed in the moving coordinate frame Γ, and that x_1' only describes the position of the origin of Γ with respect to Γ'. Therefore, x_1' can be treated as a constant in the integration.

The development of $\Delta u_{\mathrm{mw}}(x_1')$ must be predicted by the large scale flow model. Consider the velocity profile $u_1(x_1', x_3)$ defined as the velocity average taken over the x_2 coordinate in the Γ coordinate frame. It is assumed that the pressure gradient is zero outside the wires and $\partial P_{\mathrm{m}}/\partial x_1'$ between them. Then, Newton's second law may be formulated for a thin slice at the position x_1':

$$\frac{\partial}{\partial t}\left\{\rho \int_{h_1(0)}^{h_2(0)} u_1 \mathrm{d}x_3\right\} = -\Delta h \frac{\partial P_{\mathrm{m}}}{\partial x_1'} - \frac{2\eta_{\mathrm{s}}}{\delta}(\overline{u}_1 - u_{\mathrm{w}}), \tag{17}$$

where $\Delta h = \Delta h(x_1') = h_2(x_1') - h_1(x_1')$, η_{s} is the apparent viscosity of the fibre suspension, δ is the typical length scale of the velocity gradient at the mix-wire interfaces, and $\overline{u}_1$ is the average of u_1 between the wires. The last term represents the momentum transfer from the two wires to the mix through viscous drag. We assume that no momentum is transferred to the fluid outside the wires. That is, $u_1 = u_{\mathrm{w}}$ when $x_3 \le h_1$ or $x_3 \ge h_2$. This simplifies the left hand side of Eq. (17) to

$$\begin{aligned}\frac{\partial}{\partial t}\left\{\rho\int_{h_1(0)}^{h_2(0)} u_1 \mathrm{d}x_3\right\} &= \rho u_\mathrm{w}\frac{\partial}{\partial x_1'}\left\{\int_{h_1(0)}^{h_2(0)} u_1 \mathrm{d}x_3 - \int_{h_1(0)}^{h_2(0)} u_\mathrm{w}\mathrm{d}x_3\right\} \\ &= \rho u_\mathrm{w}\frac{\partial}{\partial x_1'}\left\{\int_{h_1(0)}^{h_2(0)} (u_1 - u_\mathrm{w})\mathrm{d}x_3\right\} \\ &= \rho u_\mathrm{w}\frac{\partial}{\partial x_1'}\left\{\Delta h(\overline{u}_1 - u_\mathrm{w})\right\}.\end{aligned} \tag{18}$$

By inserting Eq. (18) into Eq. (17), we obtain

$$\Delta h\frac{\partial}{\partial x_1'}\left\{\frac{\Delta u_\mathrm{mw}}{u_\mathrm{w}}\right\} + \frac{\mathrm{d}\Delta h}{\mathrm{d}x_1'}\frac{\Delta u_\mathrm{mw}}{u_\mathrm{w}} = -\frac{\Delta h}{\rho u_\mathrm{w}^2}\frac{\partial P_\mathrm{m}}{\partial x_1'} - \frac{2\eta_\mathrm{s}}{\rho u_\mathrm{w}\delta}\frac{\Delta u_\mathrm{mw}}{u_\mathrm{w}}, \tag{19}$$

where all terms are non-dimensional. The viscous term of the right-hand side is notoriously difficult to estimate for pulp fibre suspensions. However, if we examine the special case $\delta \ll \Delta h$, we find that the velocity profile is almost flat in the bulk of the mix: $u_1 \approx u_\mathrm{w} + \Delta u_\mathrm{mw}$. Therefore, the only force field acting upon the bulk is that of the pressure gradient, thus ensuring that the Bernoulli equation is satisfied. Then, Eq. (19) gives

$$\frac{2\eta_\mathrm{s}}{\rho u_\mathrm{w}\delta} = -\frac{\mathrm{d}\Delta h}{\mathrm{d}x_1'}. \tag{20}$$

That is, the boundary layer thickness δ self-adjusts to exactly decelerate or accelerate the fluid to u_w before it passes through the wires. In the other extreme, the flow is dominated by viscous effects and more similar to two-dimensional channel flow. That is, the velocity profile is parabolic. Under those conditions $\delta = \frac{1}{6}\Delta h$. In the present simulations, the boundary layer thickness δ is computed using Eq. (20), the Bernoulli boundary layer solution. If that solution exceeds $\frac{1}{6}\Delta h$, the parabolic profile solution is employed instead.

The apparent viscosity is assumed to be a function of the concentration c. It is also assumed that $h_1(x_1')$, $h_2(x_1')$, $c(x_1')$, and $P_\mathrm{m}(x_1')$ are given. An example of how these functions can be approximated is presented in Sec. 3 for the former configuration considered in this work.

3 SIMULATIONS

In this section, the unknowns of the forming model proposed in previous Sec. 2.2 are quantified for the forming configuration considered in this paper. This includes the initial condition as well as the parameters of the large scale flow model.

3.1 Initial conditions

The initial condition, corresponding to the state of the suspension at the headbox nozzle exit, consists of the initial fibre configuration and the initial velocity field $v_0(x)$. These are difficult to determine experimentally. In this work, we have chosen to combine measurements with models.

Each fibre is associated with n properties, such as length, diameter, wall thickness, stiffness, curl index, and so on. To capture interdependence of all these properties, the fibre furnish is represented by an n-dimensional probability distribution. It is too challenging, however, to experimentally measure the full distribution. In this work, the PulpEye™ fibre analyser was used to obtain the three-dimensional probability distribution of length, diameter, and curl index. The other fibre properties were regarded as independent. For each of these, a narrow distribution was chosen around a mean value obtained from the literature. Descriptions of the sample furnishes used in this work have been compiled in Appendix A. In order to reduce the computational demand, all particles smaller than 200 μm were excluded from the furnish description in most of the simulations.

To create the initial fibre configuration, fibres were drawn from the statistical furnish description, and each fibre was assigned a position drawn from a randomly uniform spatial distribution. The fibre orientation was drawn from the distribution derived in the one-dimensional headbox model proposed by Olson and co-workers [29, 30]. The input parameters of their model are the jet speed, headbox contraction ratio, and length of the headbox nozzle. These parameters are generally available. To model the effects of turbulence, Olson and co-workers also introduced a rotary diffusion of the fibres, with the dispersion coefficient $D_p = 2\ s^{-1}$. Its value was determined by fitting the model to experiments conducted on an laboratory headbox without vanes. The initial fibre configuration represents a well dispersed state with no flocculation. Concentration variations spontaneously develop during the simulation of the jet. In reality, of course, the mix is flocculated to some degree at the slice lip. The effect of this initial flocculation is neglected in the present simulations, but can be incorporated with ease given the spatial correlations of the fibres. Emerging flocculation measurement techniques

[31] may be able to provide such data at a sufficiently high resolution ($\leqslant$1 mm).

The velocity field v_0 at the nozzle tip is created by letting a given velocity field v_0' evolve into a state of fully developed turbulence, using the fluid model described in Sec. 2.1.1. Here, we have chosen the field

$$\begin{aligned} \boldsymbol{v}_0'(\boldsymbol{x}) &= v_0' \big(\sin^3 x_1' \sin^2 x_2' \sin^2 x_3' (\cos x_3' - (\lambda_1/\lambda_2)\cos x_2')\hat{\boldsymbol{e}}_1 + \\ &\quad \sin^2 x_1' \sin^3 x_2' \sin^2 x_3' (\cos x_1' - (\lambda_2/\lambda_3)\cos x_3')\hat{\boldsymbol{e}}_2 + \\ &\quad \sin^2 x_1' \sin^2 x_2' \sin^3 x_3' (\cos x_2' - (\lambda_3/\lambda_1)\cos x_1')\hat{\boldsymbol{e}}_3\big) \qquad (21a) \end{aligned}$$

$$x_i' = \frac{2\pi(x_i - a_i)}{\lambda_i}, \quad \lambda_i = \frac{b_i - a_i}{\lfloor \frac{1}{2} + (b_i - a_i)/L_\Omega \rfloor}, \quad i = 1, 2, 3. \qquad (21b)$$

This field satisfies the boundary conditions as well as the continuity condition. For a sufficiently large constant v_0', a flow will develop following Kolmogorov and Obukhov's $k^{-5/3}$-law in the inertial subrange. Other types of flow agitation can be investigated by choosing different functions for v_0', but that is outside the scope of the present investigation.

3.2 Large scale flow parameters

The input parameters of the large scale flow model are the functions $h_1(x_1')$, $h_2(x_1')$, $c(x_1')$, and $P_\mathrm{m}(x_1')$. In this section, it is described how each one of these functions can be approximated for the particular forming configuration considered in this work.

Ideally, $h_1(x_1')$ and $h_2(x_1')$ should be obtained by measuring the volumetric fluxes of suspension through the wires in the machine. Such detailed data is usually not available. It is, however, easy to measure and to some degree control the total amount of fluid drained in different sections of the machine. Measurements of the amount of drained fluid over each drainage element have been compiled in Appendix B. Therefore, $h_1(x_1')$ and $h_2(x_1')$ are known with good accuracy in the points A to I of Fig. 5. We proceed to consider the variations of $h_1(x_1')$ and $h_2(x_1')$ between those points in more detail.

The variations of $h_1(x_1')$ and $h_2(x_1')$ on the forming roll was approximated using the following method: A pressure drop develops over the wires due to their motion. This pressure drop is the sum of the structural pressure exerted by the fibres on the wires and the hydrodynamic drag exerted by the fluid on the wires. These components are readily available during simulations, and the pressure drop can be computed. An iterative procedure was used to find the functions $h_1(x_1')$ and $h_2(x_1')$ so that the typical shape of the dewatering pressure P_m was reproduced.

The dewatering over the blades was assumed to be proportional to the pressure drop over the wires. The shape of the pressure variations $P_m(x_1')$ over each blade was set according to the predictions of Roshanzamir *et al.* [32]. The maximum pressure of each blade can be controlled or measured. In these simulations, the blade pressure was set in accordance with the operating conditions described in Appendix B.

A constant rate, one-sided drainage was assumed over the suction box, as well as the couch roll. In the preliminary investigations, it was evident that the mix-to-wire speed difference downstream of the blade section was very close to zero, indicating that the network at that point is immobilised. Therefore, the $P_m(x_1')$ does not affect lateral flow beyond th point E in Fig. 5.

To determine $c(x_1')$, it was assumed that the volume concentration c_d of the drained suspension was independent of x_1'. We obtain

$$c(x_1') \approx \frac{c_0 \Delta h_0 - c_d \Delta h(x_1')}{\Delta h_0 - \Delta h(x_1')}, \tag{22}$$

where c_0 is the initial volume concentration and Δh_0 is the jet thickness at the impingement point. The apparent viscosity is assumed to be a function of the concentration c. An estimate of $\eta_s(c)$ for wood fibres suspended in water was obtained by fitting a second degree polynomial to the experimental data of Silveira *et al.* [33] for pine fibre suspensions. Due to the history-dependence of the rheological properties of fibre suspensions, the relation $\eta_s(c)$ should be regarded as a very coarse estimate. Although these estimates of the global parameters are approximate, the features of the forming mechanism are not altered, as discussed later.

3.3 Sample simulation

For the sample simulation, which is also used for comparisons with real paper in later Sec. 4.4, we use process parameters retrieved from a paper mill. The machine speed was 1500 m/min, and the jet-to-wire speed ratio was 1.02. The grammage of the paper produced in the mill was 86 g/m^2, but since fillers (15% by mass) were excluded from the furnish description of the simulations, the target basis weight of the simulated sheet was set to 77 g/m^2. Details of the operating conditions are compiled in Appendix B. The fibre furnish was composed from 60% pine kraft pulp, and 40% birch kraft pulp (see Appendix A). It was diluted to 0.7% consistency.

Since fines and fillers were excluded, the retention will be very high. In order to determine the retention, and thus c_d, a simulation was first performed with $c_d = 0$, that is 100% presumed retention. The simulated total

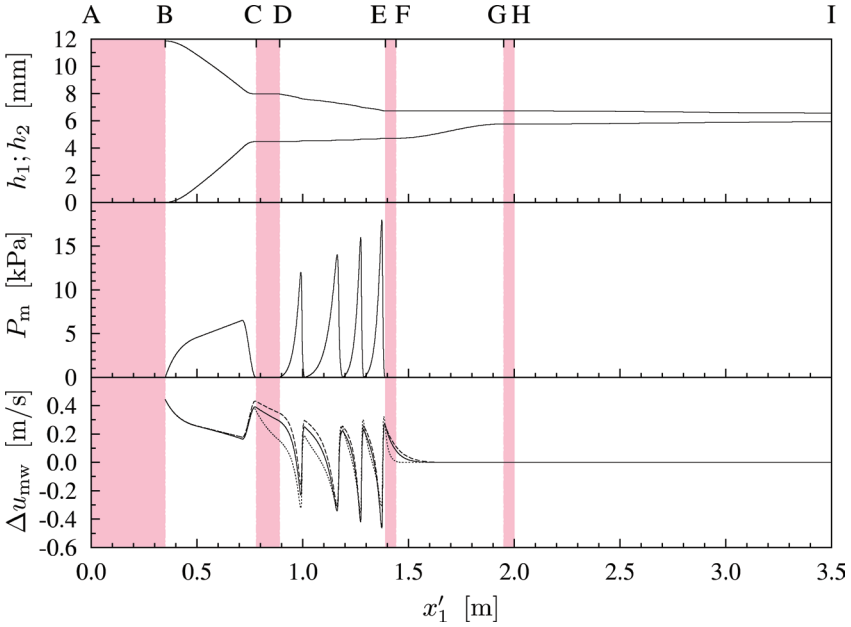

Figure 7. Sample control parameters of the large scale flow model. The positions of the wires $h_1(x_1')$ and $h_2(x_1')$, and the pressure in the mix $P_m(x_1')$ have been plotted against the position x_1' in the former. The estimated mix-to-wire speed difference $\Delta u_{mw}(x_1')$ based on the viscosity–consistency relation measured by Silveira *et al.* (see Ref. [33]) has been plotted as a solid line. The same computations but with half (dashed line) and double (dotted line) the viscosity were included for comparison. The letters at the top indicated the corresponding position in Fig. 5.

fibre retention (92%) was used to compute the real value of c_d, which was used in all further simulations.

The functions $h_1(x_1')$, $h_2(x_1')$, $P_m(x_1')$, and $\Delta u_{mw}(x_1')$ were obtained from measurements and models, as plotted in Fig. 7. The mix-to-wire speed difference was plotted for three different choices of the viscosity–consistency relation: the one measured by Silveira *et al.* [33], and half and double that value for comparison. Changing this viscosity relation did not create any fundamental change in the mix-to-wire speed difference on the forming roll or the blades.

4 RESULTS AND DISCUSSION

The results presented in this section were obtained from simulations performed according to the description in previous Sec. 3. One parameter at a time was changed in the parametric studies below.

4.1 Simulated dewatering

We begin by examining the development of the sheet structure by the eye. A simulation was conducted to create a 10 × 11 mm size paper using the process parameters described in Sec. 3.3. Figure 8 shows a series of snapshots of the mix at the points A–E and I of Fig. 5. The line of view is in the cross direction. A randomly uniform suspension, the initial state, is seen at point A. As previously mentioned, the effects of the initial flocculation was neglected. Instead, the interactions between fibres and fluid in the jet cause flocculation, leading to concentration variations at point B. After drainage on the roll, near point C just before the drop to atmospheric pressure, the flocculated state of the suspension persists. The solids concentration has increased through the thickness of the mix. There is only a very weak indication of an

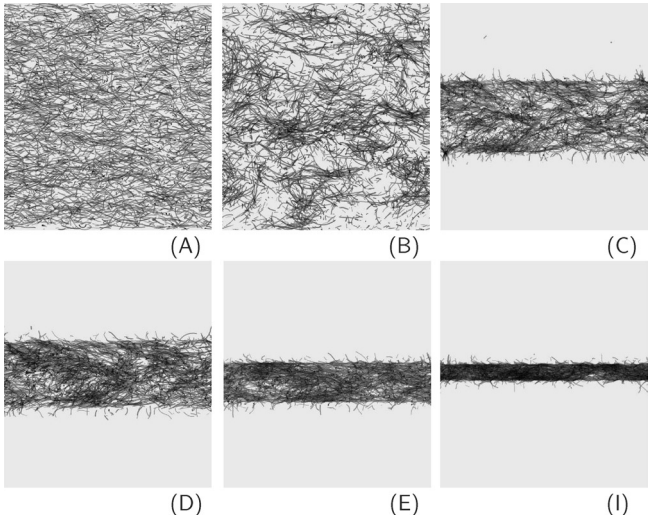

Figure 8. The simulated fibre configuration development along the length of the forming section. Images A to I correspond to positions A to I in Fig. 5. Each image is a projection of a 1.5 mm thick slice of suspension. The machine direction is to the right. The image height, and thus the jet thickness, is 12 mm.

elevated concentration near the wires. At point D, after the drop to atmospheric pressure, it is not possible to see any significant change in the structure by the naked eye. At points E and I we see only the obvious consolidation of the network.

Two different processes for formation of the fibre network were proposed by Parker [34]: *Filtration*, in which filter cakes form on the wires while the solids concentration in the bulk of the suspension remain constant, and *thickening*, in which the concentration of the mix is uniform through the thickness of the sheet during dewatering. In reality, dewatering is a combination of those two processes. One striking feature of the simulation of drainage is that no clear concentration gradient can be seen in the thickness direction (see Fig. 8). In this sample simulation, the concentration increased almost uniformly through the thickness of the mix during drainage. This is in contradiction to the conventional view that filtration is the dominant dewatering mechanism. Instead, thickening appears to dominate the dewatering process. In later Sec. 4.3, however, we shall see that filtration dewatering sometimes appears at lower headbox consistencies.

We may also examine the in-plane concentration variations by the eye. Figure 9 shows a series of snapshots of the mix with the machine direction to the right and the cross direction upward. As noted before, the structure of the initial state is randomly uniform (point A). The fibre–fluid interactions of the flow induce some small scale concentration variations (point B). Larger scale

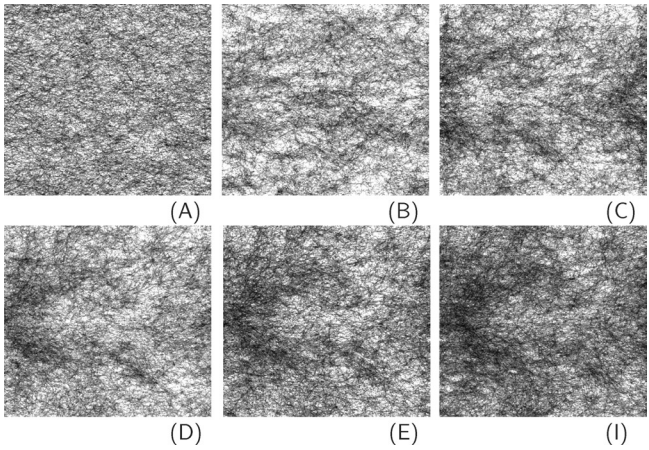

Figure 9. The simulated development of the area density variations. Images A to I correspond to positions A to I in Fig. 5. The machine direction is to the right. The image height, and thus the cross directional width, is 10 mm.

concentration variations, in the order of several millimetres, are created on the forming roll (point C). These concentration variations persist during the drop to atmospheric pressure after the forming roll (point D). Subsequent drainage over the blades, suction box and couch roll does not appear to improve formation.

It has been shown experimentally, that the large-scale formation (wavelength interval 3 mm to 30 mm) is usually improved by the blades [35]. This effect was not seen in the simulations. All flow structures in the order of the simulation box size (~10 mm) and above are attenuated. Therefore, the flow structures that may have the potential to improve large scale formation are not accounted for with the present system size. As for small-scale formation (wavelength interval 0.3 mm to 3 mm), experiments show that it is either unaffected or impaired by blade dewatering [35, 36]. This finding is in agreement with the simulation results.

4.2 Development of the fibre orientation anisotropy

A polar plot of the average fibre orientation distribution for the sample simulation is given in Fig. 10. We choose to quantify the fibre orientation anisotropy q with one of the more widely used measures [37]. A general ellipse is fitted to the data points of the polar plot, and the anisotropy is taken as $q = 1 - \beta/\alpha$, where α and β are the major and minor half-axes, respectively. With this definition $q \in [0,1)$. The simulated fibre orientation anisotropy shown in Fig. 10 does not exhibit the contraction at the ellipse minor (the

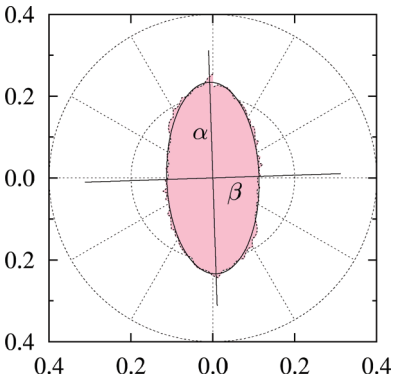

Figure 10. A polar plot of the fibre orientation distribution (dotted line). A general ellipse has been least-square fitted to the polar plot. Its half-axes α and β are used for the definition of the fibre orientation anisotropy $q = 1 - \beta/\alpha$.

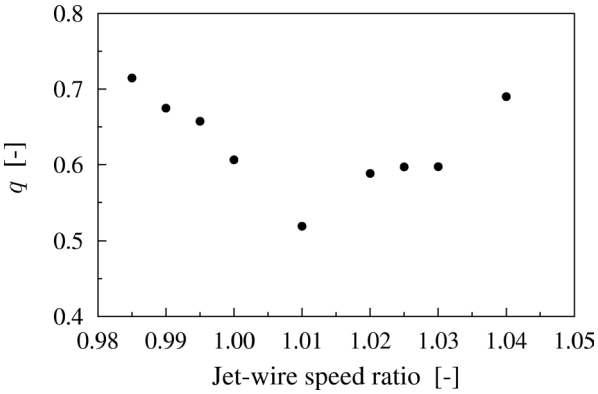

Figure 11. Simulated fibre orientation anisotropy as a function of the jet-to-wire speed ratio.

peanut shape), which is usually found in experiments. However, simulations under different conditions—lower/higher jet-to-wire speed ratio or greater consistency—did reproduce the peanut shape.

Simulations were performed in accordance with the sample simulation described in Sec. 3.3, but with a varying jet-to-wire speed ratio in the range 0.99 to 1.04. The different amounts of shear introduced in the mix is reflected in the fibre orientation anisotropy. Figure 11 shows the predicted variation of fibre orientation with the jet-to-wire speed ratio. We see that the typical behaviour, with an anisotropy minimum slightly above the ratio 1.00, is reproduced by the simulation. More insights in this variation of the anisotropy can be gained by considering its development along the length of the former.

The mix was numerically split into three layers of equal total solids contents: the top, middle and bottom layer. The development of the fibre orientation anisotropy along the length of the former was computed for each layer. The data is presented in Fig. 12. The sudden drop of the fibre orientation anisotropy at the very beginning of the free jet simulation is an artifact of the initial conditions. The headbox model we use [30] produces a highly aligned suspension, because the model has not been calibrated to include the effect of fluid agitation by the vanes of the headbox. The anisotropy reduction in the jet is due to the interaction of the aligned fibres with the initial fluid flow field described in Sec. 3.1. We note that, at this particular consistency and basis weight, the fibre orientation anisotropy develops mainly on the forming roll, while subsequent drainage elements have little effect.

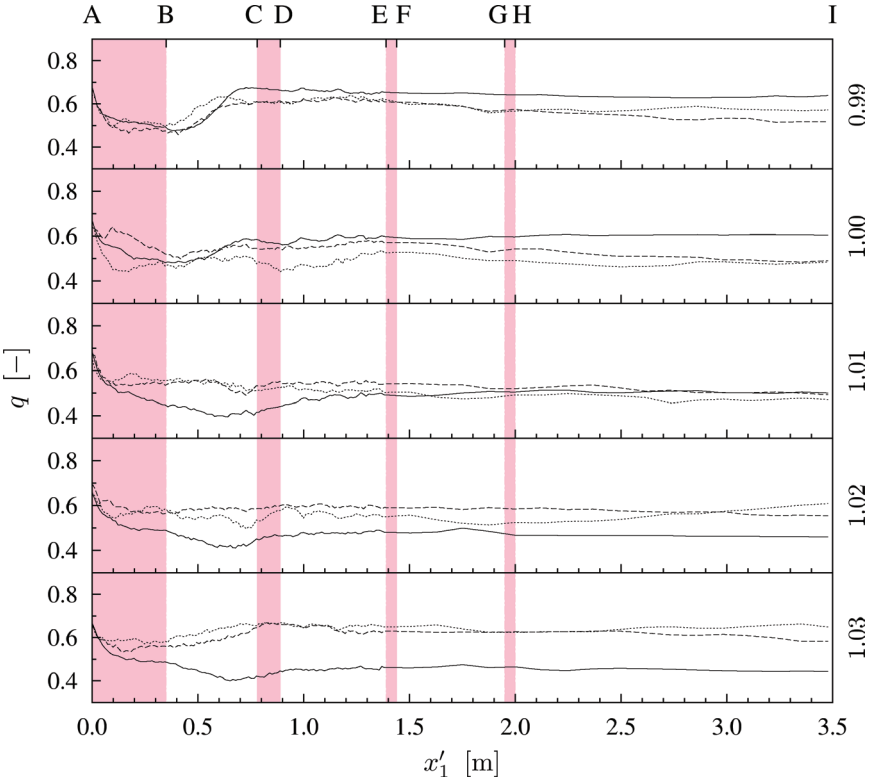

Figure 12. The mix was numerically split into three layers, top, middle and bottom, with equal basis weight. The dashed, solid, and dotted lines represent the fibre orientation anisotropy in the top, middle, and bottom layer, respectively. The development of the anisotropy was obtained for different values of the jet-to-wire speed ratio. The letters A to I refer to positions in the former (see Fig. 5).

Further examination of Fig. 12 reveals that the anisotropy of the outer layers is fairly constant during the whole forming process in the range 1.00–1.02 of the jet-to-wire speed ratio. Outside this range, the outer layers tend to become more aligned due to the increased amount of shear introduced into the mix. The middle layer shows a different behaviour. When the paper machine is run in drag, there is a rather strong alignment of the middle layer fibres on the forming roll. Conversely, in rush conditions, the forming roll acts to reduce the alignment of middle layer fibres. However, just after the forming roll, after the drop to atmospheric pressure, the middle layer fibres become

slightly more aligned in the machine direction again, because of the shear associated with the mix-to-wire speed difference caused by the sudden acceleration of the mix.

The features of the fibre orientation anisotropy profiles are in agreement with the experimental findings of Erkkilä *et al.* [37], that under drag conditions the centre of the sheet has the maximum anisotropy, while in rush there is a local minimum in the centre. Erkkilä *et al.* relate the anisotropy profile to the flow conditions during dewatering using the theory of inclined filtration [34], in which layers of fibres are immobilised as filter cakes form on the wires. According to the simulations, immobilisation of the fibre network takes place rather late in the dewatering process. In some instances the structure of the outer layers change over the entire length of the forming roll, which represents 75 % of the drainage. It may be possible to further develop the approach of Erkkilä *et al.* by taking this more detailed knowledge of the structure development into account.

4.3 Effects of basic forming parameters

Parametric studies were performed for the consistency and basis weight. In order to understand, in depth, the effects of these basic forming parameters, the analysis was focused on their impact on the process itself, and the *development* of the paper structure, rather than only the final sheet structure.

4.3.1 Consistency

Since the rheological properties of fibre suspensions vary greatly with concentration, it is reasonable to suspect that the very mechanisms of paper structure development, and the effect of different drainage elements could vary as well. In this section, we investigate the effects of consistency on the development of the through-thickness concentration gradient and fibre orientation anisotropy along the length of the former.

In Fig. 13, the development of the through-thickness concentration gradient on the forming roll and the blade section has been plotted for different mass consistencies $c_m \in \{0.3\%, 0.5\%, 0.7\%, 1.2\%\}$ at the same target basis weight (50 g/m^2). The corresponding crowding factors [38], as computed from the mass-weighted average fibre length and coarseness, were $N_c \in \{23, 38, 53, 91\}$, while typical headbox consistencies are usually in the range $20 < N_c < 60$ [39]. A clear concentration gradient is seen on the forming roll (mid BC) for the lowest consistency, and greatest jet thickness. The density of the network formed by the fibres near the wires is three times that of the bulk. However, at the end of the forming roll (point C), material is pushed into the bulk

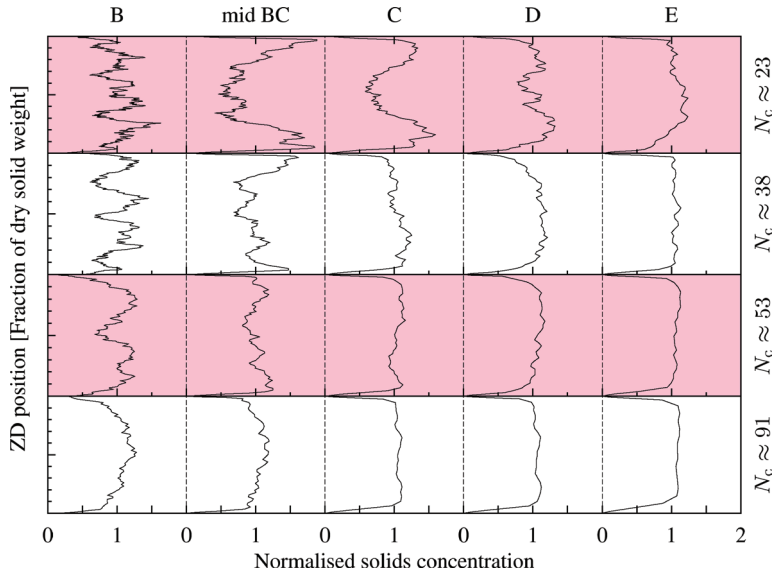

Figure 13. The development of the through-thickness concentration gradient on the forming roll and the blades for different values of the crowding factor and a constant target basis weight (50 g/m^2). The concentration has been normalised so that the integral under each curve is 1. The letters B, C, D and E refer to positions in the former (see Fig. 5).

producing a more uniform density. After the drop to atmospheric pressure (point D), the solids concentration is essentially uniform. The disruption of the network is due to the large shear introduced into the mixture by its acceleration relative to the wires. Figure 13 shows that the thickening mechanism operates in most of the dewatering process, except at the very lowest consistencies used in industrial papermaking.

Presently, the solids concentration gradient in the gap between the wires is not accessible experimentally. In a laboratory environment, an experimental technique is under development which enables the observation of the pulp suspension geometry and flow during dewatering with a pressure pulse. The fibres are labelled with Lithium atoms and monitored using Nuclear Magnetic Resonance (see Tanaka *et al.* [40]). Dewatering measurements with sufficient resolution to resolve the concentration gradient are within reach.

The through-thickness fibre orientation anisotropy was computed along the length of the forming section at different headbox consistencies. In Fig. 14, the anisotropy of the top, middle and bottom layer of the sheet has been

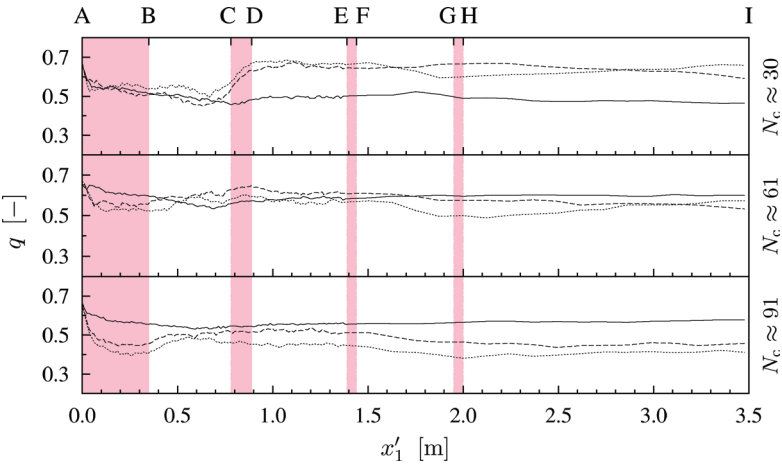

Figure 14. The sheet was numerically delaminated into three layers, top, middle and bottom, with equal basis weight. The dashed, solid, and dotted lines represent the fibre orientation anisotropy in the top, middle, and bottom layer, respectively. The development of the anisotropy was obtained for different values of the crowding factor and a constant target basis weight (50 g/m^2). The letters A to I refer to positions in the former (see Fig. 5).

plotted as functions of the position x_1' along the length of the former. Indeed, it is seen that the anisotropy development is different at different consistencies. The data was obtained at $c_m \in \{0.4\%, 0.8\%, 1.2\%\}$, which correspond to $N_c \in \{30, 61, 91\}$. These are referred to as low, medium, and high consistency, respectively. The target basis weight was 50 g/m^2 in all three cases, kept constant by varying the jet thickness.

At a low consistency (the top sub-plot), the anisotropy of all three layers is reduced in the jet and on the forming roll. After the peak pressure on the forming roll, there is a drop to atmospheric pressure. At this take-off point, the mix is accelerated leading to large shear rates near the wires. This induces alignment of the fibres in the top and bottom layers, while the middle layer is unaffected. Subsequent drainage elements have a minor effect on the anisotropy. The final paper structure shows great through-thickness anisotropy variations, with a high anisotropy in the top and bottom layers.

At a medium consistency (the middle sub-plot), the anisotropy of the middle layer is reduced in the jet and on the forming roll, while the drop to atmospheric pressure induces some alignment of the fibres. This behaviour is

similar to that of low consistency. The outer layers, however, behave differently: The forming roll slightly increases the anisotropy of those layers. It is also seen that the final phase of consolidation over the suction box and the couch roll slightly reduces the fibre orientation anisotropy. The final structure is quite uniform with respect to anisotropy. This level of consistency is also closest to the preferred operating window at the mill.

At a high headbox consistency (the bottom sub-plot), the anisotropy of the middle layer of the suspension is only slightly reduced in the jet and on the forming roll. The anisotropy of the outer layers, however, is much reduced in the jet. The core of the suspension forms a plug, forcing the agitation of the fluid to the surfaces of the jet. During the very initial phase of drainage on the roll, the shear induces anisotropy in the outer layers. Then, the mobility of the fibres is reduced, so that no further anisotropy increment is seen on the roll or the blades. The suction box tends to decrease the anisotropy of the outer layers at high headbox consistencies. This should *not* be interpreted as a possibility to modify the anisotropy of the sheet using the suction box. The effect is more likely associated with the microscale rearrangement of fibres during the transition from a three-dimensional to a two-dimensional network structure.

From Fig. 14, it is seen that consistency has a dramatic effect on the paper structure development. At a low consistency, the network formed on the forming roll is too weak to withstand the forces of the fluid as it is accelerated by the drop to atmospheric pressure, resulting in strong alignment of the surface layers. At higher consistencies, the drop to atmospheric pressure hardly affects the structure at all. It is sometimes suggested that, during filtration dewatering, fibres are deposited onto the wires to form fibre mats which are immobilised. That is, the structure of the filter cakes is preserved during subsequent drainage. In these simulations we see the opposite: When the consistency is low enough for filter cakes to develop on the forming roll, the structure is especially susceptible to shear induced by drainage elements at later stages of forming. Particularly, there is no evidence of the presence of an immobilised layer of fibres near the wires on the forming roll.

There are some observations in the literature regarding the effects of the pressure gradient where the wires leave the forming roll. It has been previously hypothesised that the shear induced by the blades may rupture the fibre network, possibly creating an adverse effect on paper strength [41, 36]. A suction pulse has also been experimentally verified at the wire take-off, which generates formation defects [42]. This observation that severe formation problems arise after the roll, even though most drainage occur on the roll, also indicates that the the partly formed fibre network is, at least sometimes, not immobilised.

4.3.2 Basis weight

In this investigation, the target basis weight was varied by adjusting the jet thickness, while the headbox consistency was maintained at a constant level of 0.7%, and the jet-to-wire speed ratio was kept at 1.02. All other process data was taken from the operating conditions of the sample simulation (see Sec. 3.3 and Appendix B).

The development of the fibre orientation anisotropy has been plotted in Fig. 15 for different target basis weights. The fibre orientation anisotropy was investigated separately for the top, middle and bottom layer of the mix.

First, consider the three papers with basis weight in the range 35–70 g/m^2. The anisotropy of the middle layer is reduced on the forming roll and unaffected of subsequent drainage elements. Its development is essentially the same irrespective of the target basis weight. The fibres of the outer layers become more aligned with the machine direction on the forming roll, and

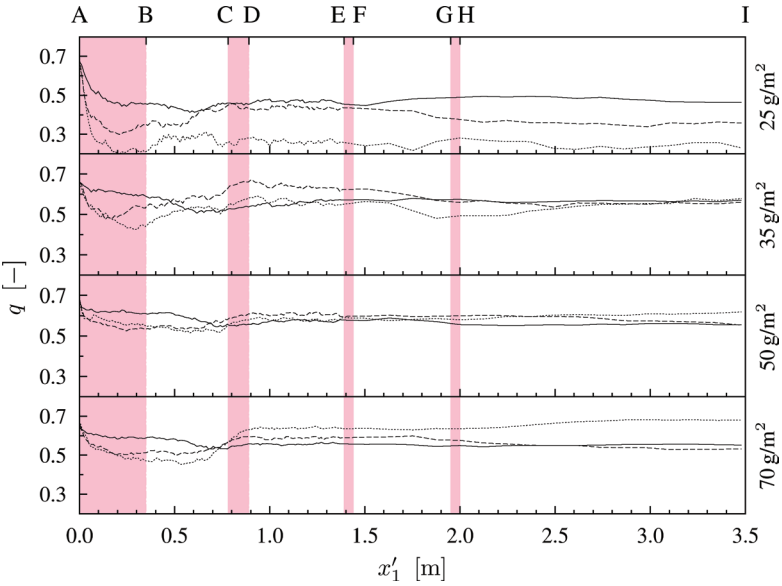

Figure 15. The mix was numerically delaminated into three layers, top, middle and bottom, with equal basis weight. The dashed, solid, and dotted lines represent the fibre orientation anisotropy in the top, middle, and bottom layer, respectively. The development of the fibre orientation anisotropy was obtained for different values of the basis weight while maintaining a constant consistency of 0.7%, and a jet-to-wire speed ratio of 1.02. The letters A to I refer to positions in the former (see Fig. 5).

also at the drop to atmospheric pressure. The anisotropy of the outer layers may increase a little with target basis weight. The basis weight has far less impact on the fibre orientation than had the consistency.

For the most light weight paper grade (25 g/m^2), the reduction of the fibre orientation anisotropy is very efficient in the turbulent jet, particularly in the outer layers. Then, the anisotropy of the outer layers increases slightly during drainage on the forming roll. The final light weight paper is more isotropic in the outer layers than in the middle layer. The over-all anisotropy is relatively low as compared to heavier grades.

4.4 Comparison of final paper structures with paper mill data

Currently, no experimental technique is available for measuring the fibre-level details of the paper structure inside the narrow gap between the wires in the former; the resolution is just below 1 mm [31]. Therefore, only the *final structure* predicted by the simulations was compared with real papers. Before this comparison is undertaken, it is appropriate to point out some differences between simulations and actual machine operation. The fibre furnish used in the simulations is composed from a mixture of hardwood and softwood fibres, but they were not sampled from the mill. Furthermore, we had no access to the fibre length distribution in the headbox or whitewater, and thus could not estimate the enrichment of fines in the headbox furnish. During normal operation at the paper mill, the furnish properties varies considerably over time, depending on the variations of raw materials, broke content, and variations in the white water circulation. There is thus a great variation in the furnish composition under normal operation. Consequently, it may be difficult to make a direct quantitative comparison between simulated sheets and sheets from the paper mill. Nevertheless, a preliminary comparison is still of interest to give an idea of the differences of simulated and real paper sheets.

The sample sheets were manufactured with the former configuration similar to what was used in the simulations (see Fig. 1). In the validation case, the machine produced an 86 g/m^2 fine paper at 1500 m/min, from a mixture of 60% softwood and 40% hardwood pulp. Further details of the operating conditions are presented in Appendix B.

Analyses were carried out for the through-thickness fibre length distribution and the through-thickness fibre orientation anisotropy. Both measurements are based on sheet splitting. The measurement for z-directional fibre orientation has been described elsewhere [43]. For z-directional fibre length distribution, the paper was laminated in a commercial hot laminator and subsequently split by hand. The laminate foils of each layer were put in deionised water for 24 hours. Then, the fibres were gently pealed off the

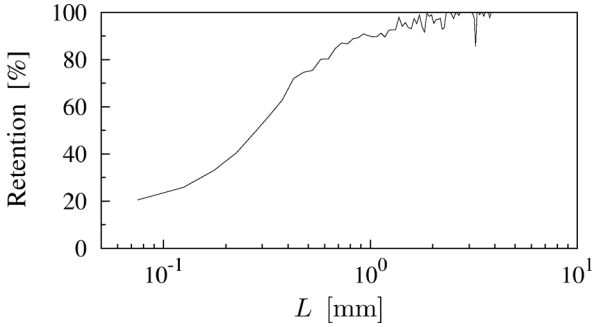

Figure 16. The simulated retention as a function of fibre length, for particles larger than 50 μm.

plastic foils. This whole procedure is known to produce a certain amount of additional debris. The suspension was disintegrated and the fibre length distribution was measured using the Kajaani FS-200 system [44]. Only particles larger than 50 μm are considered in our analysis due to the limited optical resolution of the FS-200.

Three 4×5 mm^2 sheets were simulated, with a particle length cutoff at 50 μm, to be used for comparisons with the sample sheets from the paper mill. The simulated retention of different length fractions (see Fig. 16) is useful for later discussion of the fibre length distribution. Almost all fibres greater than 0.5 mm are retained. The normalised initial and final fibre length distribution of the simulations and the fibre length distribution of the sample sheets are plotted in Fig. 17. When comparing the initial and final length distribution of the simulation, it is seen that the share of the smallest particles ($L < 200$ μm) have been reduced, thus increasing the share of larger particles. The discrepancies between the length distribution of the simulated sheets and the sample sheets arose partly because the fibre furnishes were different, as described above. However, they may also reflect differences in the the retention of small particles.

The through-thickness distributions of small particles in the simulated sheets were computed between the wire surfaces. That is, it was assumed that the small particles trapped inside the voids of the wires will not be included in the web as it leaves the forming section. Figure 18 shows that particles in the length range 200–400 μm give a uniform distribution through the thickness in the simulated sheets, as well as the sample sheets. The frequency differs, because the pulps did not have an identical length distribution. The frequency of particles in the range 50–200 μm show a local minimum in the centre of the

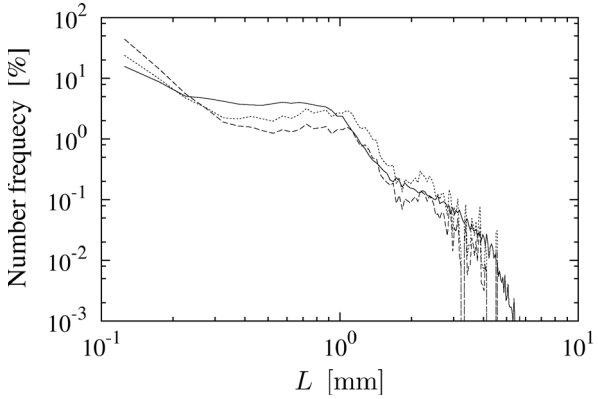

Figure 17. The initial fibre length distribution (dashed line) of the simulation, the fibre length distribution of the simulated sheet (dotted line), and the fibre length distribution of the reslushed, non-delaminated sample sheets (solid line).

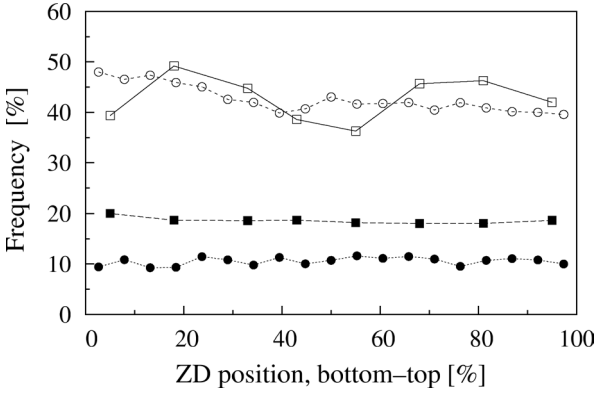

Figure 18. The through-thickness frequency of fines in the delaminated sample sheets (squares) and the simulated sheets (circles). The ZD position is given as a fraction of the basis weight. The open symbols represent particles in the length range 50–200 μm, while the filled symbols represent particles in the range 200–400 μm.

sample sheets. This is not visible in the simulated sheets. The reason for this discrepancy is not known at this moment.

The total anisotropy of the three simulated sheets was $q = 0.50 \pm 0.03$, with a sample size of 0.22 cm^2. The sample sheets were 25 cm^2 and obtained far from the machine edges. The anisotropy of the sample sheets were 0.45.

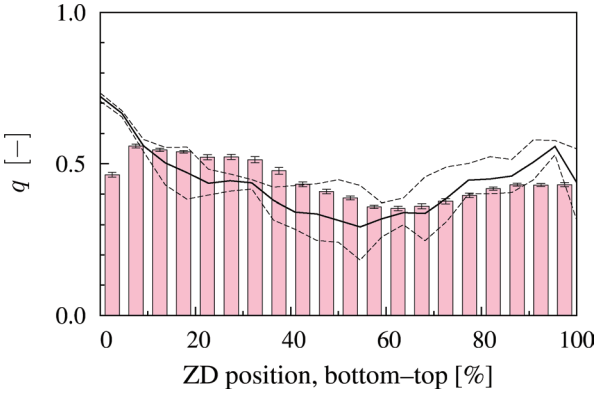

Figure 19. The through-thickness fibre orientation anisotropy of real paper sheets (bars), with error bars representing the standard error based on six different samples. These are compared with the simulated fibre orientation anisotropy (solid line), which is an average taken over three simulations. The dotted lines indicate the maximum and minimum values. The ZD position is given as a fraction of the basis weight in the case of simulated sheets, and as the layer number for real sheets.

Considering the mix-to-wire speed variations over the width of the web and other naturally occurring process variations, a 0.05 difference in fibre orientation anisotropy units is not unexpected.

The through-thickness fibre orientation anisotropy of the simulated sheets and the sample papers are compared in Fig. 19. The simulations agree with the real sheets that the outer layers are more anisotropic than the inner layers. Considering the small sample size of the simulated sheets, the agreement is fair except at the very bottom layer of the sheet, where simulations overpredict the fibre orientation anisotropy. The origin of this discrepancy is unknown.

5 CONCLUSIONS

A theoretical framework for particle-level simulation of forming was given. Fibres are modelled as flexible discrete objects interacting with each other, as well as the suspending fluid. Newton's second law was used for integrating the fibre motion, while the Navier–Stokes equations was used for the fluid motion. Drainage is simulated by introducing two model forming fabrics moving toward each other through the mix.

The model was used to simulate forming in a former configuration similar

to the Voith DuoFormer™ TQv [2]. The development of the through-thickness fibre length distribution and fibre orientation distribution along the length of the former was observed. Parametric studies of the jet-to-wire speed ratio, consistency, and target basis weight were performed.

Under the forming conditions examined in this work, the through-thickness concentration gradient was almost uniform throughout the forming process. The dewatering mechanism could thus be characterised as thickening rather than filtration. Filtration dewatering was also observed, but only in the lower range of papermaking consistencies.

It was found that the single most important drainage element, in terms of impact on the paper structure, is the forming roll. It was observed that drainage on the forming roll introduced in-plane basis weight variations in the sheet. It was also shown that the fibre orientation anisotropy of both the inner layers and surface layers develops mainly on the forming roll. In some instances, at small consistencies and a large jet thickness, the drop to atmospheric pressure immediately after the forming roll has a dramatic effect on the paper structure. The fibre network near the wires yields and is subjected to shear, with an increased alignment of fibres in the surface layers as a result.

The effects of varying the consistency and the basis weight were investigated separately. It was shown that changes in the consistency can have strong effects on the through-thickness fibre orientation anisotropy. The paper structure development is less sensitive to the basis weight, except for the most light-weight grades, which are sensitive to the flow conditions in the jet.

There is a large set of potentially important process parameters, whose variation may affect the paper structure in different ways depending on the current operating window. The proposed forming model can be used to systematically investigate which parameters are important, and how the parameters inter-relate to produce the final paper structure.

A STOCK PROPERTIES

The mass-weighted mean values of some properties of pulps A (pine kraft pulp) and B (birch kraft pulp), excluding all particles whose length falls below the limit 200 μm. Fibre length, diameter and curl index were measured by the PulpEye™ fibre analyser, the coarseness was estimated from the data presented by Retulainen *et al.* [45], the wall thickness was calculated from the mean diameter, mean coarseness and the assumption that the density of solids were, 1500 kg/m^3, and the wet stiffness values are magnitude estimates based on the data provided by Kerekes and Tam Doo [46].

Property	*Pine kraft pulp*	*Birch kraft pulp*
Length	1.87 mm	0.97 mm
Diameter	28.9 μm	25.4 μm
Curl index	0.087	0.050
Coarseness	0.26 mg/m	0.14 mg/m
Wall thickness	1.8 μm	1.1 μm
Wet stiffness	3×10^{-12} N $\cdot$ m^2	2×10^{-12} N $\cdot$ m^2

B OPERATING CONDITIONS

This section contains a lists of the relevant operating conditions used in the simulations of this work. All process parameters and data were obtained from a paper mill producing a fine paper.

Machine data	
Grammage (15% fillers)	86 g/m^2
Machine speed	1500 m/min
Jet/wire ratio	1.02
Furnish data	
Hardwood	40%
Softwood	60%
Filler in headbox	5 g/l
Headbox data	
Slice opening	12 mm
Channel height after tube bank	140 mm
Length of nozzle	720 mm
Distance to impingement point	350 mm
Consistency	1.0%

Drainage element data	
Forming roll radius	700 mm
Wire tension	4.8kN/m
Forming roll wrapping angle	35°
Number of blades	4
Blade pressure	120–200 mbar
Conc. after couch roll	20%
Volume fraction drained	
Forming roll top side	35%
Forming roll bottom side	40%
Blade section	13%
Suction box	9%
Couch roll	3%

REFERENCES

1. S. B. Lindström and T. Uesaka. Particle-level simulation of forming of the fibre network in papermaking. *Int. J. Eng. Sci.*, **46**:858–876, 2008.
2. Voith DuoFormer™ TQv product sheet, http://www.voithpaper.com.
3. H. P. G. Darcy. **Les fontaines publiques de la ville de Dijon**. Victor Dalmont, Paris, 1856. pp. 590–594.
4. K. A. Landman, C. Sirakoff, and L. R. White. Dewatering of flocculated suspensions by pressure filtration. *Phys. Fluids A*, **3**:1495–1509, 1991.
5. T. Bando, T. Adachi, and H. Iwata. Drainage mechanism on a twin-wire former (Part 2) Computer simulation on pulsating drainage. *Jpn Tappi J.*, **48**:96–102, 1994.
6. D. M. Martinez. Characterizing the dewatering rate in roll gap formers. *J. Pulp Pap. Sci.*, **24**:7–13, 1998.
7. V. Lobosco, B. Norman, and S. Östlund. Modelling of forming and densification of fibre mats in twin-wire formers. *Nordic Pulp Pap. Res. J.*, **20**:16–23, 2005.
8. C. Holmqvist, A. Dahlkild, and B. Norman. A flexible approach for modelling flow in multi-component blade formers. *Nordic Pulp Pap. Res. J.*, **21**:73–81, 2006.
9. K. Niskanen and M. J. Alava. Planar random networks with flexible fibres. *Phys. Rev. Lett.*, **25**:3475–3477, 1994.
10. C. Barratte, J.-C. Roux, C. Voillot, J.-F. LeNest, J.-C. Lonjon, and P. J. Mangin. Paper structure simulation: Forming fabric input. In proc. *27th EUCEPA conference – Crossing the millennium frontier, emerging technical and scientific challenges*, pp 125–130, Grenoble, France. 1999.

11. L. H. Switzer, D. J. Klingenberg, and C. T. Scott. Handsheet formation and mechanical testing via fibre level simulations. *Nordic Pulp Pap. Res. J.*, **19**:434–439, 2004.
12. C. F. Schmid, L. H. Switzer, and D. J. Klingenberg. Simulations of fibre flocculation: Effects of fibre properties and interfibre friction. *J. Rheol.*, **44**:781–809, 2000.
13. S. B. Lindström and T. Uesaka. Simulation of the motion of flexible fibres in viscous fluid flow. *Phys. Fluids*, **19**:113307, 2007.
14. S. B. Lindström and T. Uesaka. Simulation of semidilute suspensions of non-Brownian fibres in shear flow. *J. Chem. Phys.*, **128**:024901, 2008.
15. W. E and J.-G. Liu. Finite difference methods for 3D viscous incompressible flows in the vorticity–vector potential formulation on nonstaggered grids. *J. Comput. Phys.*, **138**:57–82, 1997.
16. G. J. Hirasaki and J. D. Hellums. A general formulation of the boundary conditions on the vector potential in three-dimensional hydrodynamics. *Q. App. Math.*, **16**:331–342, 1968.
17. M. Lesieur and O. Métais. New trends in large-eddy simulations of turbulence. *Ann. Rev. Fluid Mech.*, **28**:45–82, 1996.
18. C. S. Peskin. Numerical analysis of blood flow in the heart. *J. Comput. Phys.*, **25**:220–252, 1977.
19. E. A. Fadlun, R. Verzicco, P. Orlandi, and J. Mohd-Yusof. Combined immersed-boundary finite-difference methods for three-dimensional complex flow simulations. *J. Comput. Phys.*, **161**:35–60, 2000.
20. G. B. Jeffery. The motion of ellipsoidal particles immersed in a viscous fluid. *Proc. Roy. Soc. London, Ser. A*, **102**:161–179, 1922.
21. F. P. Bretherton. The motion of rigid particles in a shear flow at low Reynolds number. *J. Fluid Mech.*, **14**:284–304, 1962.
22. R. G. Cox. The motion of long slender bodies in a viscous fluid. Part 2. Shear flow. *J. Fluid Mech.*, **45**:625–657, 1971.
23. G. I. Taylor. The motion of ellipsoidal particles in a viscous fluid. *Proc. Roy. Soc. London, Ser. A*, **103**:58–61, 1923.
24. E. Anczurowski and S. G. Mason. Particle motions in sheared suspensions. XXIV. Rotation of rigid spheroids and cylinders. *Trans. Soc. Rheol.*, **12**:209–215, 1968.
25. S. Kim and S. J. Karrila. **Microhydrodynamics: Principles and selected applications**. Butterworth–Heinemann, 1991.
26. S. Yamamoto and T. Matsuoka. Dynamic simulation of fibre suspensions in shear flow. *J. Chem. Phys.*, **102**:2254–2260, 1995.
27. Y. Yamane, Y. Kaneda, and M. Doi. Numerical simulation of semi-dilute suspensions of rodlike particles in shear flow. *J. Non-Newtonian Fluid Mech.*, **54**:405–421, 1994.
28. G. Joseph, R. Zenit, M. Hunt, and A. Rosenwinkel. Particle-wall collisions in a viscous fluid. *J. Fluid Mech*, **433**:329–346, 2001.
29. J. A. Olson. Analytic estimate of the fibre orientation distribution in a head-box flow. *Nordic Pulp Pap. Res. J.*, **17**:302–306, 2002.
30. J. A. Olson, I. Frigaard, C. Chan, and J. P. Hämäläinen. Modelling a turbulent

fibre suspension flowing in a planar contraction: The one-dimensional headbox. *Int. J. Multiphase Flow*, **30**:51–66, 2004.
31. D. Söderberg and C. Holmqvist. A novel system for online wet-end web monitoring. In proc. *PaperCon '08. Sustainability: profits and performance for the pulp, paper and board industries*, Dallas, US. TAPPI, 2008.
32. A. Roshanzamir, S. I. Green, and R. J. Kerekes. Two-dimensional simulation of pressure pulses in blade gap formers. *J. Pulp Pap. Sci.*, **24**:364–368, 1998.
33. M. T. Silveira, A. G. M. Ferreira, and L. Q. Lobo. The viscosity of aqueous suspensions of cellulose fibers. Part 1. Influence of consistency and fiber length. *Silva Lusitana*, **10**:171–178, 2002.
34. J. D. Parker. **The sheet forming process**. TAPPI, Atlanta, GA, 1972.
35. B. Nordström and B. Norman. Effects of roll-blade and roll forming on formation, retention, mechanical properties and anisotropy—a preliminary comparison. *J. Pulp Pap. Sci.*, **21**:J223–J230, 1995.
36. B. Nordström. Twin-wire blade forming versus roll forming of a linerboard furnish—effects on tensile strength and formation. *Nordic Pulp Pap. Res. J.*, **18**:245–254, 2003.
37. A.-L. Erkkilä, P. Pakarinen, and M. Odell. Sheet forming studies using layered orientation analysis. *Pulp Pap. Can.*, **99**:T39–T43, 1998.
38. R. J. Kerekes and C. J. Schell. Characterisation of fibre flocculation regimes by crowding factor. *J. Pulp Pap. Sci.*, **18**:J32–J38, 1992.
39. R. J. Kerekes. Rheology of fibre suspensions in papermaking: An overview of recent research. *Nordic Pulp Pap. Res. J.*, **21**:598–612, 2006.
40. S. Tanaka, S. Dvinskikh, F. Lundell, I. Furó, and L. D. Söderberg. Flow measurements in fibre suspension by NMR. In proc. *Svenska mekanikdagarna*, Luleå, Sweden. 2007.
41. B. Nordström and B. Norman. Effects on paper properties and retention of the proportion of roll dewatering during twin-wire roll-blade forming of TMP. *J. Pulp Pap. Sci.*, **22**:J283–J289, 1996.
42. B. Norman, L. Hermansson, and D. Söderberg. The new STFI-former. In proc. *PulPaper*, Helsinki, Finland. Finnish Paper Engineers' Association, 2007.
43. U. Hirn and W. Bauer. Evaluating an improved method to determine layered fibre orientation by sheet splitting. In proc. *Int. Paper Phys. Conf.*, pp71–80, Gold Coast, Australia. 2007.
44. S. C. Young. A calibration and maintenance schedule for the Kajaani FS-200 fibre analyser. *Appita J.*, **46**:435–438, 1993.
45. E. Retulainen, K. Niskanen, and N. Nilsen. Fibres and bonds. Ch. 2 in **Paper Physics** (ed. K. Niskanen), nr 16 in Papermaking Science and Technology, p59. Fapet Oy, second edition, 1998.
46. R. J. Kerekes and P. A. Tam Doo. Wet fibre flexibility of some major softwood species pulped by various processes. *J. Pulp Pap. Sci.*, **11**:60–61, 1985.

EVOLUTION OF THE PAPER STRUCTURE ALONG THE LENGTH OF A TWIN-WIRE FORMER

Stefan B. Lindström,[1] *Tetsu Uesaka*[1]* and *Ulrich Hirn*[2]

[1]Department of Natural Sciences, Engineering and Mathematics, Mid Sweden University, Holmgatan 10, 851 70 Sundsvall, Sweden
[2]Institute of Paper, Pulp and Fibre Technology, Graz University of Technology, Kopernikusgasse 24, 8010 Graz, Austria
*Current affiliation: FPInnovations – Paprican Division, 570 St. John Boulevard, Pointe-Claire, Quebec, Canada H9R-3J9

PREPARED DISCUSSION CONTRIBUTION

Daniel Söderberg – Innventia and KTH – Royal Institute of Technology

Background

The presented paper has very ambitious goals with a focus of understanding the effects of basic process parameters such as grammage and concentration as well as the effect of drainage elements on paper microstructure. In order to achieve the goal, a modelling approach is made where a multiple-scale model is implemented. The model contains two parts, one part that models the large-scale machine direction (MD) variation and one that models the behaviour on the small-scale between the forming fabrics. In order to perform the simulation, the MD pressure variation, distance between the forming fabrics and thus concentration is given based on experimental data and ad-hoc assumptions. The potential and use of the small-scale model has been published previously and also employed in simulation of twin-wire forming [1].

As a starting point it is stated that "With the particle-level model for

forming simulation, every detail of the evolving paper structure is available for analysis along the length of the forming section. This opens up the possibility to investigate a variety of questions critical to papermakers." Specifically, the paper is concerned with:

- What are the effects of individual drainage elements on the paper microstructures?
- How do changes in the basic parameters, grammage and consistency, modify the paper microstructures?

Response

Overall the paper represents an impressive effort to develop a tool that tries to model the influence of forming parameters on paper structure. However, the starting point for this response is the conclusions of the paper that state the following:

- Newton's second law was used for integrating the fibre motion, while the Navier–Stokes equations were used for the fluid motion
- It was found that the single most important drainage element, in terms of impact on the paper structure, is the forming roll:
  - introduces in-plane basis weight variations in the sheet
  - fibre orientation anisotropy of both the inner layers and surface layers develops mainly on the forming roll
- The proposed forming model can be used to systematically investigate which parameters are important, and how the parameters inter-relate to produce the final paper structure

In my opinion these conclusion are maybe not fully supported neither by the methodology and results of the paper nor previously published work. Therefore comments on each of these conclusions follow.

Conclusion: Newton's second law was used for integrating the fibre motion, while the Navier–Stokes equations were used for the fluid motion

This statement seems to indicate that the full set of governing equations was used in the simulations and that no further assumptions have been made. This is not supported by the description of the simulation methodology used as stated in the paper. In order to allow large Reynolds numbers, a sub-grid turbulence model was used. The behaviour of the turbulent flow on the sub-grid scale is thus prescribed by a simple model. As indicated in the paper, the presence of fibres will have an effect on the flow behaviour on this scale. It is also noted that this effect is outside the scope of the paper. However, in order

to estimate the effect, there is actually good available data showing the impact of fibres on the turbulent dissipation.

Bennington and Mmbaga [2] showed that fibres change the nature of dissipation of the turbulent energy. In a turbulent fibre suspension, the turbulent energy is not dissipated to heat at small scales, as it is in pure water. Instead, the dissipation occurs due to fibre-fibre interaction. The experiments were performed in a high-intensity mixer and the viscous dissipation ε was measured by analyzing the end product of a reaction between two chemicals. A model of chemical reactivity was applied, which coupled the result of the analysis to the viscous dissipation.

Results from this study are shown in Figure 1. In Figure 1 the relative liquid-phase dissipation, $\varepsilon/\varepsilon_0$ is plotted as a function of concentration. The viscous dissipation, ε, is given by the experiment, i.e. the chemical reaction, and ε_0 is given by the input power to the mixer.

In the graph it is obvious that viscous dissipation is strongly influenced by the presence of fibres. For a fibre volume concentration of 0.01, the viscous dissipation accounts for about 50 % of the total but, in contrast, for the polyethylene beads, attenuation is only 10 % at the same volume concentra-

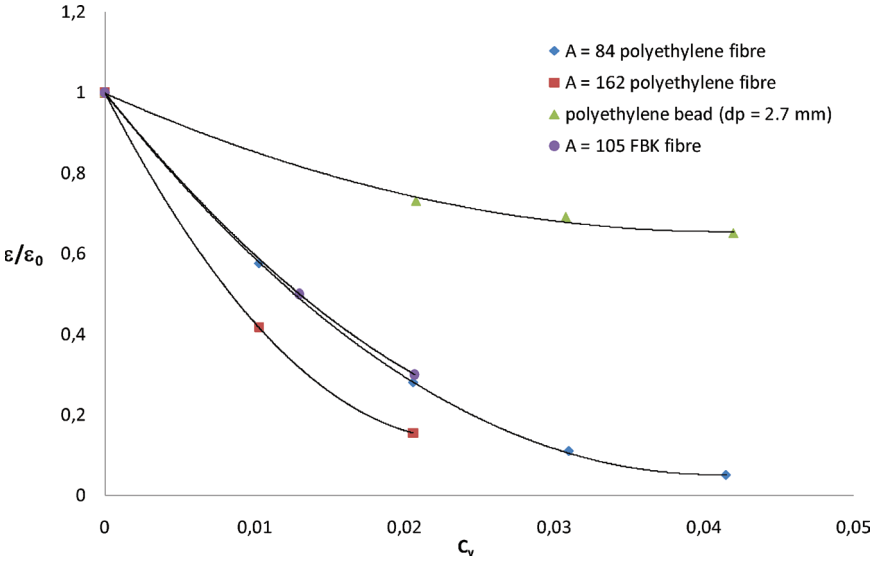

Figure 1. Relative liquid-phase energy dissipation versus volumetric concentration for fibres of different aspect ratios and for a suspension of polyethylene beads. Data taken from [2]. (FBK=Fully Bleached Kraft pulp).

tion. For the low aspect-ratio polyethylene fibres and the FBK pulp the attenuation is similar. For the high aspect-ratio polyethylene fibres attenuation is even stronger.

The experiments, which were performed at given impeller speeds, showed a variation in power input depending on fibres and concentration. This could be argued to be a source for the differences between the suspensions. However, results were also presented regarding the effect of rotational speed for an FBK pulp, which showed that, although there is an effect of rotational speed, it is weak compared to the effect of concentration.

This result clearly shows that assumption of the suspension behaving as water on the small-scale (Kolmogorov scale) is far from correct. Instead energy is consumed by a constant break-up of the flocs followed by re-flocculation. The conclusion is therefore that flocculation and turbulent decay will be significantly different from what is predicted by the presented model. It is also suggested that these experimental data could be used to tune the model allowing more accurate predictions.

Conclusion: It was found that the single most important drainage element, in terms of impact on the paper structure, is the forming roll

From the results of the simulations it is argued that formation degradation, i.e. in-plane basis weight variation, is introduced by the forming roll. However, this conclusion is most probably a result of poor initial conditions.

It was clearly shown by Kerekes *et al.* [3], that turbulence both disrupts and creates fibre flocs. Although shear forces in a turbulent flow-field have the capability to disrupt fibre flocs, turbulence also creates flocs. In a continuous turbulent flow, fibre flocs will continuously be disrupted followed by re-flocculation. This is supported by several studies; see, for example, [2] and [3]. The presented simulation results are only a result of the initial conditions, i.e. the upstream boundary conditions. At the headbox slice, which forms the upstream boundary, fibre flocculation is not present in the simulations and turbulence level is defined by simulating a pure water flow at the given velocity, i.e. Reynolds number. The result of this is a very high level of turbulent fluctuations.

Based on results presented by Parsheh and Dahlkild [4], turbulence is clearly damped by the headbox contraction. Their results, which are based on measurements in a flow without fibres, clearly show that the absolute level of the turbulent fluctuations never exceeds the level going into the headbox contraction. Assuming that the contraction ratio of the headbox is 10 and that the turbulent fluctuations are 10% of the mean flow velocity at the beginning of the contraction they are reduced to <1% at the slice.

As seen by, for example, Lundell and Söderberg [6], fibres will also have a significant turbulence dampening effect. Since neither the effect of headbox contraction nor fibres are taken into account, the initial condition for the turbulent state at the slice is most likely at least an order of magnitude too high.

In Figure 2 a visualisation of the flocculation state in a headbox jet is shown taken from [7]. This is a figure representing a time-sequence captured at high speed. If the images in the series are analysed, there seems to be no visible re-distribution of fibres, which indicates a very low turbulence level. In addition, the images also show clearly that the suspension is flocculated.

Based on these results, it is suggested that the conclusion that in-plane basis-weight variation is introduced on the forming roll is only a result of poorly chosen boundary (initial) conditions. The assumption of a non-flocculated state at the slice is incorrect and if the flocculation state and the

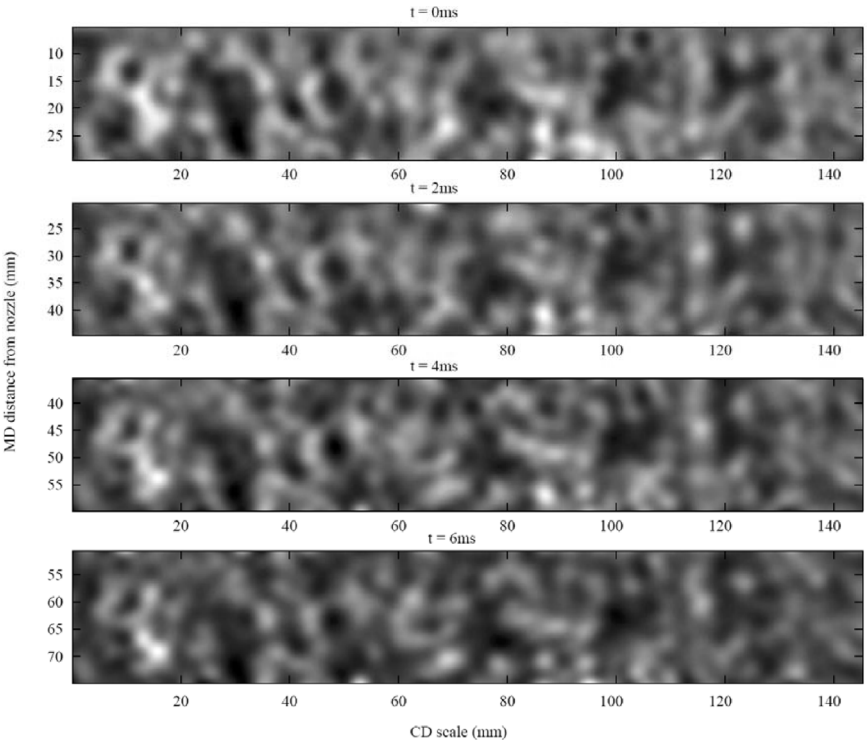

Figure 2. Time sequence of the headbox jet at 7.5 m s^{-1} with a fibre suspension. The images follow the flow, which can be seen on the vertical axes [7].

level of turbulent fluctuations were adequately chosen this effect would not be seen. It is therefore suggested that the forming roll will have little or no impact on formation. This is under the assumption that the pressure profile is "well-behaved", without significant pressure pulses.

Conclusion: The proposed forming model can be used to systematically investigate which parameters are important, and how the parameters inter-relate to produce the final paper structure

This is of course the goal for the development of the presented model. However, based on the discussion above, it is suggested that more work needs to be done in order to be able to draw conclusions based on the simulations. Specifically, more experimental verifications have to be made and the large-scale model has to be further developed to accurately predict pressure variation in the MD.

REFERENCES

1. S. B. Lindström and T. Uesaka. Particle-level simulation of forming of the fibre network in papermaking. *Int. J. Eng. Sci.*, **46**:858–876, 2008.
2. C.P.J. Bennington and J.P. Mmbaga, Liquid-Phase Turbulence in Pulp Fibre Suspensions, in **The Science of Papermaking**, *Trans. 12th Fund. Res. Symp.*, pp255–283, Oxford, 2001.
3. R.J. Kerekes, R.M. Soszynski and P.A. Tam Doo, The Flocculation of Pulp Fibres, In **Papermaking Raw Materials**, *Trans. 8th Fund. Res. Symp.*, pp265–310, Oxford, 1985.
4. H. Karema, J. Salmela, M. Tukiainen and H. Lepomaki, Prediction of Paper Formation by Fluidization and Reflocculation Experiments, in **The Science of Papermaking**, *Trans. 12th Fund. Res. Symp.*, pp559–589, Oxford, 2001.
5. M. Parsheh and A. Dahlkild, Numerical modelling of mixing in a stratified headbox jet, in proc. *Tappi Engineering Conference*, pp1159–1173, Nashville. Tappi Press 1997.
6. F. Lundell, D. Söderberg, S. Storey and R. Holm, The Effect of Fibres on Laminar-Turbulent Transition and Scales in Turbulent Decay, in **Advances in Paper Science and Technology**, *Trans. 13th Fund. Res. Symp.*, pp19–34, Cambridge, 2005.
7. L.D. Söderberg, A comparison between the flow from a paper machine headbox and a low Reynolds number water jet, in proc. *Tappi Engineering Conference*, pp 1155–1172, Anaheim. Tappi Press 1999.

GENERAL DISCUSSION

Steve Keller Miami University

Daniel, could you go back a couple of slides there to your image of formation? Can you give me an indication of the scale differences between the image you are showing here and what Stefan was showing for formation in his study?

Daniel Söderberg

In this case, this is 1 cm and Stefan simulates 1 cm. These are very long fibres in the visualisation.

Steve Keller

Do you think that the scale differences between the flocs that you are looking at, and the changes that Stefan might be seeing at his scale, could account for the differences in conclusions?

Daniel Söderberg

I do not believe that, since I would expect that the crowding number was about the same for this as for Stefan's results, which would be governing the mobility of fibres.

Steve Keller

I guess what I am looking for is that if you have the capability of focusing in on individual fibres, would you see them move? What you are looking at are coarse flocs which one would expect not to have that type of mobility.

Daniel Söderberg

I took it away, you see the red square? There is actually a follow-up on this slide where this box is imaged at higher resolution and you still do not see any motion. Actually, you do not see any motion in this first part of the jet, then suddenly, at a distance from the slice, you get a lot of motion because the jet become unstable and creates turbulence by itself.

Discussion

Steve Keller

Does that account for what Stefan was seeing, as you move that box?

Daniel Söderberg

That is not part of the model, the instability of the jet.

Stefan Lindström

No, the simulation box only spans the size of one such floc. In order to investigate how the forming section affects these flocs, it would be necessary to include at least 2 floc sizes inside the simulation box – one dense part and one less dense. Probably, an even greater size of the simulation box is required.

Kit Dodson University of Manchester

Would it be fair to say, if we could see the movie here, that we would see a variation in that red box that is roughly like the variation we see along the top of your image?

Daniel Söderberg

You mean that the time variation would be the same order as the spatial variation. Yes, I guess so.

Kit Dodson

Thank you. The other query is that Stefan said that he was working with fine paper. It is difficult to believe that this head box is going to deliver fine paper. So it may be you discuss different things in this context.

Daniel Söderberg

Yes, but it is amazing! I would say that you would get very nice paper! We have done a lot of jet imaging both at the pilot scale and at mills, and it looks much worse in the head box and better than you could ever imagine when you look at the final paper.

Ari Kiviranta M-real (from the chair)

Yes. I'll just make a comment about what Daniel is saying. I completely agree with him, it is unbelievable how bad the jet can look and yet still you can produce good paper.

Kit Dodson

I think that is very interesting. Thank you very much.

Mark Martinez University of British Columbia

Before I ask my question, you need to clarify something first. In your simulations, it is a fluid structure interaction problem, but you used as an input the gap size as a function of position, is that correct?

Stefan Lindström

Yes.

Mark Martinez

So here's the question – I do not understand this. The big picture is that you have a gap size which is symmetric: it is an axisymmetric problem you are looking at. Your inlet condition is a uniform concentration and your outlet condition is a uniform concentration, but right in the middle, you have a region of a very complex concentration profile and symmetry is broken in that region. So the question I have is: what is causing the symmetry to be broken in the middle of the forming zone?

Stefan Lindström

The speed of the two wires in the thickness direction is not the same. So you drain asymmetrically, so the simulation is not symmetric.

Lars Wågberg KTH

Thank you, first of all, both of you for a great discussion. However, I want to bring a bit more chemistry into this discussion and I would like to ask how you are modelling the fibre interactions in your model?

Discussion

Stefan Lindström

In this case, they are purely mechanical, so there is a frictional force with an effective coefficient of friction, which I took from one of Dick Kerekes' review papers and, of course, there is the possibility of having any type of potential force between these fibers, which I have not included yet. So the model is presenting only friction and hydrodynamic interactions.

Lars Wågberg

I was thinking about what Agne Swerin showed us in his PhD Thesis. He showed that the critical number fibre–fibre contacts for creating a fibre network went down from 3 to 1.2, when you added chemicals. Maybe that kind of approach could be used in your model.

Stefan Lindström

It will be interesting to try it and see what happens.

Jean-Claude Roux University of Grenoble

In your simulation, did you change the location of the counter blades and, if you did that, did you obtain any interesting information?

Stefan Lindström

I did not attempt that. I obtained the blade interspacing from the data sheet of the Voith DuoFormer. But I think that we would get interesting results only if we increased the size of the simulation box because the interesting thing about the blades is that they affect flocculation, and they affect the formation of the final paper, particularly the large scale formation.

Jean-Claude Roux

But they may also affect fibre orientation. I do not totally agree with you when you say that filtration mechanism cannot be obtained. It depends on the location of the "wet line". We have also an equivalent wet line on a twin wire machine as your machine – it depends on the processing parameters. You may have some filtration mechanism which is followed by thickening or by pressing because it is effectively wet pressing between two wires.

Stefan Lindström

Yes, of course, there is a certain range only within which I have varied the process parameters; but the properties of the pulp can change a lot and so on and I have to investigate each individual case. The system is so complex that it is very difficult to draw general conclusions, and we really have to try different drainage strategies and process parameters, so that is a good comment.

Ilya Vadeiko FPInnovations

I have a question concerning fines distribution. You show that there is a discrepancy between the experiment and the model. I was wondering if the fine particles are allowed to escape from you systems with the draining water or not?

Stefan Lindström

Yes.